



Influences of ENSO and intraseasonal oscillations on distinct tropical cyclone clusters over the western North Pacific

Yitian Qian¹ · Pang-Chi Hsu¹ · Hiroyuki Murakami² · Jianyun Gao³ · Huijing Wang¹ · Mingkeng Duan¹

Received: 13 May 2023 / Accepted: 13 October 2023 / Published online: 4 November 2023
© The Author(s), under exclusive licence to Springer-Verlag GmbH Germany, part of Springer Nature 2023

Abstract

Although the influences of El Niño–Southern Oscillation (ENSO) and boreal summer intraseasonal oscillation (ISO) on basin-wide tropical cyclone (TC) activity over the western North Pacific (WNP) have been widely recognized, how the seasonal and subseasonal anomalies of sea surface temperature and atmospheric ISO variations modulate different types of WNP TCs needed further examination, as addressed in this study. Using a fuzzy *c*-means clustering method, we objectively classified the WNP TCs into seven distinct clusters with different genesis locations and trajectories. The genesis numbers of all seven TC clusters revealed significant spectral variance at the intraseasonal timescale in the bands of 10–30 and 30–90 days. Based on the diagnosis of scale-decomposed genesis potential index, we found that the increase in ISO-related mid-tropospheric moistening plays the most important role in TC genesis for all seven clusters, while anomalous circulations (low-level vorticity and mid-level vertical motion) are secondary. The trajectories associated with straight-moving and recurving TC clusters are modulated by ISO-related steering flows. These modulations of TC activities by ISO vary with the phase of ENSO. The modulations of ISO are significantly greater for TCs generated in the southeast quadrant of the WNP in El Niño years than in La Niña years, while ISO imposes a larger impact on landfalling TCs occurring in La Niña years, which are changed by the low-level winds associated with ENSO conditions. The compound effects of ENSO and ISO on TC clusters provide useful sources of subseasonal TC predictability. Our statistical model using the information of ENSO and ISO shows skillful predictions of WNP TC genesis numbers and track distributions at the lead time up to 30 days.

Keywords Tropical cyclone · Intraseasonal oscillation · ENSO · Cluster analysis · Subseasonal prediction · Western North Pacific

1 Introduction

Tropical cyclones (TCs) are one of the costliest natural disasters affecting coastal regions over much of the world (e.g., Pielke et al. 2008; Smith and Katz 2013). Owing to

its warm sea surface temperature (SST), abundant moisture, and large-scale cyclonic circulation of the monsoon trough, the western North Pacific (WNP) is the region with the highest TC occurrence, accounting for 30% of the TCs over all ocean regions globally (e.g., Gray 1968; McBride 1995). The activities of TCs over the WNP are strongly influenced by natural variabilities with different timescales. At the interannual timescale, the TC genesis location, number, track, and intensity are modulated by SST anomalies associated with the El Niño–Southern Oscillation (ENSO) (Chia and Ropelewski 2002; Wang and Chan 2002; Camargo et al. 2007a) and Pacific Meridional Mode (Zhang et al. 2016a; Murakami et al. 2017). As the dominant mode of subseasonal variability, the phase evolution and intensity of boreal summer intraseasonal oscillation (ISO) also influence the activities of WNP TCs (Li and Zhou 2013a, b; Zhao et al. 2015). Increased (decreased) TC genesis numbers are observed during the active (inactive) phase of ISO when the

✉ Pang-Chi Hsu
pangchi@nuist.edu.cn

¹ Key Laboratory of Meteorological Disaster, Ministry of Education (KLME)/Collaborative Innovation Center On Forecast and Evaluation of Meteorological Disasters (CIC-FEMD)/Joint International Research Laboratory of Climate and Environment Change (ILCEC), Nanjing University of Information Science and Technology, Nanjing, China

² Geophysical Fluid Dynamics Laboratory, Princeton, NJ, USA

³ Fujian Key Laboratory of Severe Weather, Fujian Institute of Meteorological Sciences, Fuzhou 350001, China

cyclonic anomaly, abundant moisture, small vertical wind shear, and deep convection provide a favorable environment for TC formation (Liebmann et al. 1994; Kim et al. 2008; Hsu et al. 2011; Li and Zhou 2013a; Zhao et al. 2015). By investigating the genesis potential index (GPI), Camargo et al. (2009) found the largest contribution to derive from the ISO relative humidity anomaly, followed by the low-level absolute vorticity (Zhao et al. 2015). The modulations by ISO on TC genesis numbers in different ENSO phases have also been discussed. Li et al. (2012) revealed an asymmetric modulation of TC genesis by the Madden–Julian Oscillation (MJO) under different ENSO conditions, with an enhanced MJO–TC relationship in El Niño years compared with La Niña years. Han et al. (2020) indicated that more TCs are generated over the WNP in active phases of the 10–30-day Quasi-Biweekly Oscillation (QBWO) in ENSO neutral years than in El Niño or La Niña years. Zhao et al. (2022) found that ENSO, and then either the MJO or QBWO, were the two most important predictors, after the climatology of TC genesis, over different sub-basins of the WNP, in their statistical intraseasonal TC forecast model.

The modulations of TCs by ENSO (along with other interannual SST anomalies) and ISO provide a physical basis for seasonal and subseasonal predictions of WNP TC activities (Gray et al. 1992, 1993, 1994; Klotzbach and Gray 2004, 2009; Klotzbach 2008; Leroy and Wheeler 2008; Vitart et al. 2010; Slade and Maloney 2013; Xiang et al. 2015; Murakami et al. 2015; Nakano et al. 2017; Jiang et al. 2018; Lee et al. 2018). Compared to seasonal TC prediction systems, which are relatively well developed (Gray et al. 1992, 1993, 1994; Camargo and Barnston 2009; Kim et al. 2012; Murakami et al. 2015, 2016a, b), subseasonal TC prediction models are still in their infancy (Leroy and Wheeler 2008; Vitart et al. 2010; Slade and Maloney 2013; Nakano et al. 2017; Jiang et al. 2018; Lee et al. 2018). In early work, Leroy and Wheeler (2008) developed a logistic regression model to predict the weekly TC genesis probability in the Southern Hemisphere based on the climatology of TC genesis numbers, the real-time multivariate MJO (RMM) index, and the two leading modes of the interannual SST variability associated with ENSO. Their statistical model showed an increased prediction skill, out to about the third week, by including MJO information, suggesting that ISO serves as an important source of TC genesis predictability at the subseasonal timescale. Following the work of Leroy and Wheeler (2008) and Slade and Maloney (2013) constructed a statistical model for intraseasonal TC genesis prediction over the Atlantic and eastern Pacific and indicated that a skillful prediction could be achieved at lead times of 2–3 weeks when the MJO index was used in the model. Note, however, that the statistical models of Leroy and Wheeler (2008) and Slade and Maloney (2013) only provided predictions of whether or not a TC would occur over these ocean basins;

they lacked information on the genesis numbers, genesis locations, and trajectories of TCs. Wei et al. (2021) constructed a similar spatiotemporal projection method (STPM) to that proposed by Hsu et al. (2015) to predict the principal components (PCs) of the MJO and QBWO. Then, they predicted the TC genesis over the South China Sea (SCS) based on the predicted PC and historical statistical relationship between the QBWO/MJO and TC daily genesis rate.

With improvements in high-resolution dynamic models in simulating ISO and its relationship with TCs (Jiang et al. 2012; Satoh et al. 2012), it has become possible to predict the generation and movement of TCs at longer lead times of several weeks (Elsberry et al. 2010; Vitart et al. 2010; Nakano et al. 2017; Xiang et al. 2015; Jiang et al. 2018; Lee et al. 2018). For instance, Elsberry et al. (2010) and Vitart et al. (2010) showed that the European Centre for Medium-Range Weather Forecasts (ECMWF) monthly forecast model can provide useful guidance for the TC genesis over the WNP and the Southern Hemisphere a few weeks in advance. Based on the high-resolution (50-km) coupled model of the National Oceanic and Atmospheric Administration/Geophysical Fluid Dynamics Laboratory (NOAA/GFDL), Xiang et al. (2015) reported that the genesis of Hurricane Sandy in the Atlantic in 2012, and Super Typhoon Haiyan in the western Pacific in 2013, could be correctly predicted with a lead time of about 11 days. Jiang et al. (2018) then extended the study of Xiang et al. (2015) by assessing the prediction skill of the GFDL forecast system for all 600+ TCs that occurred during 2003–2013. They found that only about 10% of the TCs were correctly predicted at a 1-week lead, indicating that subseasonal TC prediction is still a challenge for state-of-the-art high-resolution coupled models. A similar conclusion was obtained by Lee et al. (2018), who evaluated the TC genesis prediction skill of six subseasonal-to-seasonal (S2S) models and found that the ECMWF S2S model performed best, with skillful predictions for TC genesis numbers in the Atlantic and WNP in the week 2 (days 8–14) forecast. The other S2S models displayed limited skill at a 1-week lead. The prediction skill for probabilistic TC occurrence at a regional scale (15° latitude × 20° longitude) over different basins was assessed by Gregory et al. (2019) and Lee et al. (2018), who both concluded that the ECMWF model shows the best skill, out to 3–4 weeks in advance. Qian et al. (2020) introduced a novel dynamical–statistical model for subseasonal TC forecasting over the WNP, with a 25-day lead time, which considers different TC clusters with distinct genesis locations and trajectories. Additional progress in the mechanisms of subseasonal variability and other operational TC prediction systems can be found in the review paper by Camargo et al. (2019).

In summary, the overall skill revealed by the operational systems is still limited (at around 2 weeks), which is because the modulation by ISO of TC subseasonal variabilities is

not yet fully understood, especially regarding the compound impacts of ISO and ENSO on different kinds of TCs over the WNP. This suggests a need to further explore efficient and useful approaches to subseasonal TC prediction. Accordingly, in this study, we investigated in greater detail the modulating effects of ISO and ENSO on different types of WNP TCs, which had been previously objectively categorized by clustering analysis (Camargo et al. 2007a, b; Chu et al. 2010; Kim et al. 2011; Zhang et al. 2016b; Zhao et al. 2018). In this previous work, Camargo et al. (2007a) briefly demonstrated the connection between the MJO phases and ENSO and each of the TC clusters. However, the detailed processes through which ISO influences distinct TC clusters, such as the relative contributions of ISO-related dynamic and thermodynamic effects on different TC clusters, have not been elucidated. Besides, with the impact of the different phases of ENSO evolution, the different modulations of ISO on different TC clusters should also be investigated. Studies have thus far mostly focused on the subseasonal prediction of TC genesis numbers, but probabilistic information concerning TC genesis locations and track patterns over the entire WNP would also be useful for risk management and policymakers. Based on results regarding the modulations by ISO and ENSO on individual TC clusters, we constructed statistical models by using the key ISO-related environmental factors in different ENSO phases as potential predictors of the genesis numbers of each TC cluster at the lead times of 10–40 days. Then, we obtained probability maps of TC frequency (TCF) by considering both the genesis number and climatological probability of TCF for individual clusters (Chu et al. 2010; Kim et al. 2011).

The rest of the paper is organized as follows: in Sect. 2, we describe the methods and data used in our study. The modulating effects of ISO on distinct TC clusters, including their genesis and trajectory patterns, as well as the different impacts of ISO on distinct TC clusters under ENSO-related large-scale fields, are examined in Sect. 3. In Sect. 4, we present the procedures of WNP TC prediction at 10–40-day leads, along with the forecast results. Conclusions and some further discussions are provided in Sect. 5.

2 Data and methods

2.1 Data

1. TC dataset

The TC genesis and track data over the WNP (0° – 60° N, 100° E– 180°) are from the Regional Specialized Meteorological Centers Tokyo-Typhoon Center best-track dataset, as archived in the International Best Track Archive for Climate Stewardship (Knapp et al. 2010). We focus on tropical storms or stronger cyclones (sus-

tained wind speed ≥ 34 knots), collectively referred to as TCs in this study.

2. Large-scale field datasets

The GPI was calculated using the large-scale fields obtained from the ERA-Interim dataset (Dee et al. 2011), which has a $1.5^{\circ} \times 1.5^{\circ}$ (latitude \times longitude) resolution. The variables used include 3-D zonal and meridional wind fields, vertical velocity, relative humidity, temperature, and geopotential height. The SST data are from the NOAA High-resolution Blended Analysis of daily SST at a $0.25^{\circ} \times 0.25^{\circ}$ (latitude \times longitude) resolution (Reynolds et al. 2007). All the large-scale fields were interpolated into a uniform resolution of $1.5^{\circ} \times 1.5^{\circ}$ (latitude \times longitude). We used daily outgoing longwave radiation (OLR) data at a horizontal resolution of $2.5^{\circ} \times 2.5^{\circ}$ (latitude \times longitude) from the polar-orbiting satellites of the National Oceanic and Atmospheric Administration (Liebmann and Smith 1996) to identify deep convection activity. The study period covers the WNP TC season (June–November) during 1982–2018.

3. Definition of ENSO state

Considering sufficient sample sizes and distinct separation of ENSO phases, the El Niño (La Niña) years are defined as when the seasonal mean (June–November) Niño-3.4 (5° S– 5° N, 170° – 120° W) SST anomaly is greater than 0.8σ (less than -0.8σ), based on the NOAA High-resolution Blended Analysis of daily SST. According to this definition, six El Niño years (1982, 1987, 1997, 2002, 2009, 2015) and ten La Niña years (1984, 1985, 1988, 1989, 1998, 1999, 2000, 2007, 2010, 2011) are defined. The remaining 21 years are neutral years. Our sensitivity test shows that the major results are not sensitive to the thresholds selected.

The forecast Niño-3.4 index [area-averaged SST over (5° S– 5° N, 170° – 120° W)] is used as the product of the North American Multi-Model Ensemble (NMME) forecasting project (Kirtman et al. 2014). Six models provide real-time Niño-3.4 index datasets, while only four models provide early predictions from 1982. Therefore, we utilized the 1-month lead real-time Niño-3.4 index products provided by these four models, including CanCM4i, CFSv2, NASA_GEOS5v2, and NCAR_CCSM4. The forecast El Niño (La Niña) phases are defined as when the real-time seasonal mean (June–November) Niño-3.4 index is greater than 0.8σ (less than -0.8σ) at a lead time of 1 month.

2.2 Methods

1. Fuzzy *c*-means clustering analysis

To objectively classify the WNP TC clusters (or track patterns), we used the fuzzy *c*-means clustering method (Bezdek 1981), which is based on minimizing an objec-

tive function of the c -means function. The mathematics of the c -means function can be found in Chu et al. (2010) and Kim et al. (2011), which highlight the superiority of the c -means clustering method in analyzing clusters with ambiguous boundaries, like TC data.

According to the results of previous studies (Camargo et al. 2007a, b; Chu et al. 2010; Kim et al. 2011; Zhang et al. 2016b), WNP TCs can be suitably classified into seven clusters, denoted by C1–C7, respectively. Figure 1 and Table 1 display their basic features, including their

genesis and center locations of trajectories, lifespans, trajectory lengths, maximum wind speeds, and accumulated cyclone energy (ACE; Bell et al. 2000). “TCall” represents all TC cases over the WNP basin. Briefly, C1 is characterized by TCs that generate and develop over the SCS and might strike southern China and the Indochina Peninsula (Fig. 1a). The TCs of C1 have the shortest lifespan (2.7 days) and trajectory length (1037.8 km), as well as the lowest maximum wind speed (64.3 m s^{-1}) and ACE ($9078 \text{ m}^2 \text{ s}^{-2}$), among the seven

Fig. 1 a–g Seven TC clusters (C1–C7) derived from the fuzzy c -means clustering method using **h** all WNP TC cases (TCall) during the TC season of 1982–2018. The red curve represents the central trajectory of TCs. The number and percentage of TCs for each cluster are listed in parentheses.

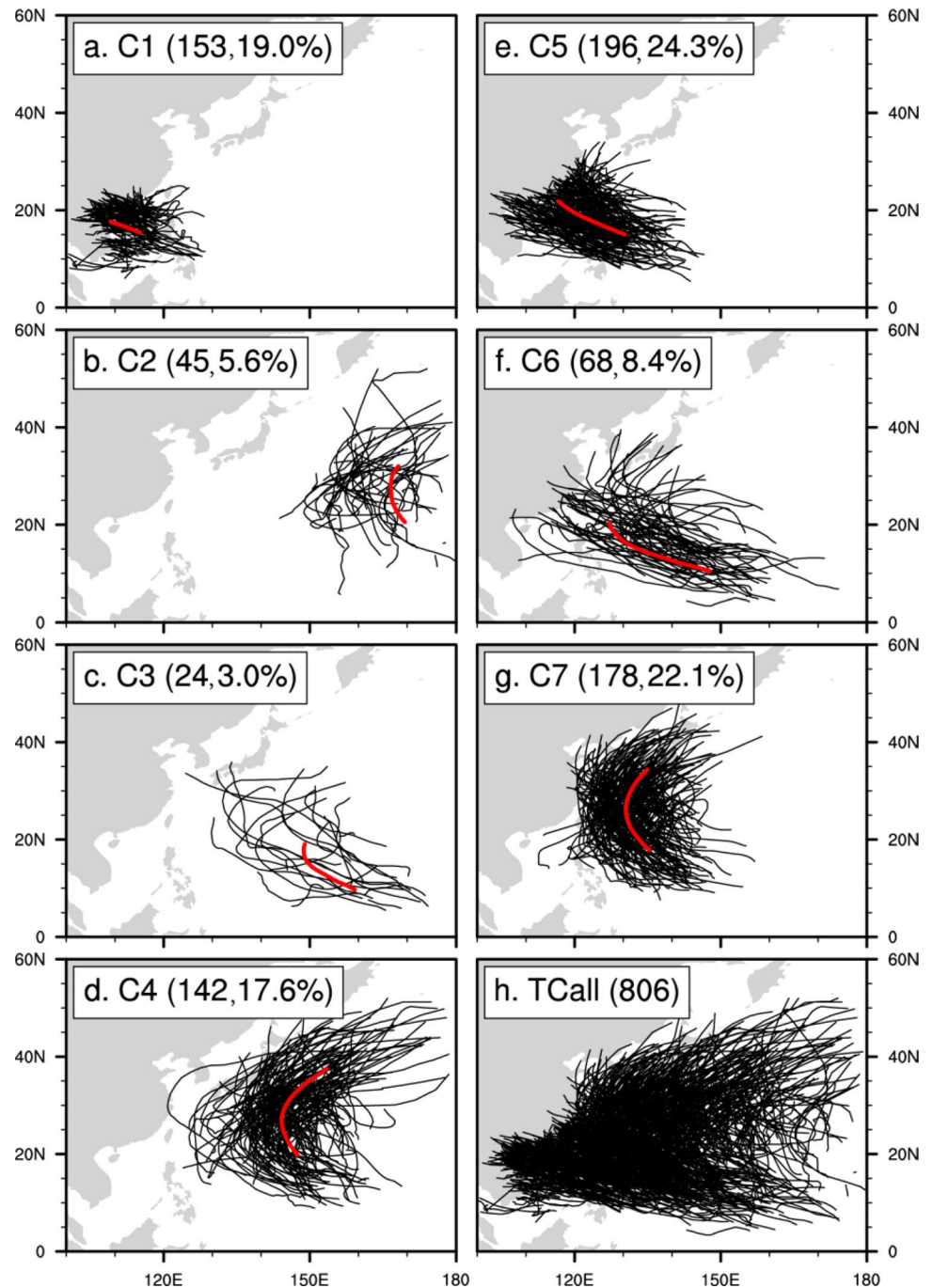


Table 1 Basic characteristics of clusters C1–C7 and all TC cases (TCall)

	Genesis location (lon, lat)	Lifespan (days)	Trajectory length (km)	Maximum wind speed (m s ⁻¹)	Accumulated cyclone energy (ACE) (m ² s ⁻²)
C1	113.2° E, 16.9° N	2.7	1037.8	64.3	9078
C2	162.4° E, 27.0° N	4.0	2284.2	74.6	19,958
C3	150.3° E, 17.7° N	6.4	3064.2	82.3	57,438
C4	145.8° E, 26.4° N	5.9	3297.0	82.3	34,991
C5	123.1° E, 18.3° N	4.9	2119.4	87.5	27,683
C6	136.8° E, 17.7° N	7.5	3734.2	87.5	63,761
C7	132.2° E, 24.0° N	5.7	2896.6	79.7	37,486
TCall	133.4° E, 21.5° N	5.1	2466.7	87.5	31,102

TC trajectory length is measured from its formation (TC sustained wind speed exceeds 17 m s⁻¹ for the first time) to dissipation (TC sustained wind speed reduces to below 17 m s⁻¹)

clusters, owing to the limited basin size of the SCS and the short distance to land. The TCs of C2 have the eastmost (162.4° E) and northmost (27.0° N) genesis locations, which form and propagate over the open ocean of the WNP without making landfall (Fig. 1b). C3 is another cluster with most TCs being active in the open ocean; however, the TCs of C3 are generated more to the south and west than those of C2 and have longer lifespans (Fig. 1c, Table 1). C4 is characterized by TCs moving northwestward and turning northeastward, which affects southeastern Japan (Fig. 1d). The TCs of C5, with straightforward and west/northwest-oriented trajectories, mostly strike Taiwan and East China (Fig. 1e). C6 is a cluster of TCs that form in the southeastern part of the WNP and has the longest lifespan and largest ACE (Table 1). Finally, the TCs of C7 are generated to the east of the Philippines and easily make landfall in South Korea and Japan.

2. Definitions of ISO activity

The boreal summer ISO consists of two different modes, with periods of 10–30 and 30–90 days. To separate the high-frequency (HF; period of 10–30 days) and low-frequency (LF; period of 30–90 days) ISO components, the Lanczos band-pass filter (Duchon 1979) was applied to the time series of OLR at each grid cell to extract the HF and LF components of intraseasonal variability. The dominant patterns of the HF/LF ISO modes over the WNP were further identified by using empirical orthogonal function (EOF) analysis of band-pass-filtered OLR over the WNP (0°–60° N, 100° E–180°) during June–November of 1982–2018. The first two leading modes of HF (LF) variability explain 7.4% (16.6%) and 5.9% (11.1%) variances, respectively. They are both statistically significant according to the North’s rule of thumb (North et al. 1982). Based on the lead-lag correlation coefficients between the first two PCs for June–November from 1982 to 2018, we find that the first mode of HF (LF) variability tends to lead the second mode by

about 4 (10) days, with a significant correlation coefficient of 0.50 (0.48), indicating that the two leading modes occur in conjunction as a pair. The amplitude and phase of the HF/LF ISO activities were then defined by the first two leading PCs (PC1 and PC2). An active LF/HF ISO day was selected when the amplitude of the HF/LF ISO [(PC1² + PC2²)^{1/2}] was greater than or equal to 1.

3. Scale-decomposed GPI

To quantitatively identify key factors associated with the ISO in modulating TC activity over the WNP, we examined the GPI (I_{GPI}) at the intraseasonal timescale over the TC genesis region based solely on the days with TC generations for each TC cluster. A modified GPI that incorporates the vertical motion effect proposed by Murakami and Wang (2010) was used in this study:

$$I_{GPI} = \left| 10^5 \zeta \right|^{3/2} \left(\frac{I_{RH}}{50} \right)^3 \left(\frac{V_{pot}}{70} \right)^3 (1 + 0.1V_s)^{-2} \left(\frac{-\omega + 0.1}{0.1} \right), \tag{1}$$

where ζ is the 850-hPa absolute vorticity (s⁻¹), I_{RH} is the relative humidity (%) at 600 hPa, V_{pot} is the TC maximum potential intensity (MPI; m s⁻¹; Emanuel 1995), V_s is the vertical wind shear (m s⁻¹) between 850 and 200 hPa, and ω is the vertical pressure velocity (Pa s⁻¹) at 500 hPa. V_{pot} was defined by Emanuel (1995) and modified by Bister and Emanuel (1998) as follows:

$$V_{pot}^2 = \frac{C_k}{C_D} \frac{T_s}{T_0} (CAPE^* - CAPE^b), \tag{2}$$

where C_k is the exchange coefficient for enthalpy, C_D is the drag coefficient, T_s is SST (K), and T_0 is the mean outflow temperature (K). The quantity $CAPE^*$ is the value of the convective available potential energy (CAPE) with reference to the surrounding environment, and $CAPE^b$ is that of the boundary layer air.

For convenience, Eq. (1) is represented by the following five terms:

$$I_{\text{GPI}} = \eta \cdot \gamma \cdot \psi \cdot s \cdot w, \quad (3)$$

where η denotes the GPI component associated with 850-hPa absolute vorticity; γ denotes the GPI term related to relative humidity at 600 hPa; ψ represents the GPI component of potential intensity; and s and w represent the GPI terms of vertical wind shear and vertical motion, respectively.

To examine the relative effects of the climatological seasonal cycle and subseasonal perturbations (mainly ISO) on the five large-scale factors of the GPI, the intraseasonal components of GPI variables are defined as follows:

$$\begin{aligned} I'_{\text{GPI}} &= (\bar{\eta} + \eta') \cdot (\bar{\gamma} + \gamma') \cdot (\bar{\psi} + \psi') \cdot (\bar{s} + s') \cdot (\bar{w} + w') - \bar{\eta} \cdot \bar{\gamma} \cdot \bar{\psi} \cdot \bar{s} \cdot \bar{w} \\ &= \eta' \cdot \bar{\gamma} \cdot \bar{\psi} \cdot \bar{s} \cdot \bar{w} + \bar{\eta} \cdot \gamma' \cdot \bar{\psi} \cdot \bar{s} \cdot \bar{w} + \bar{\eta} \cdot \bar{\gamma} \cdot \psi' \cdot \bar{s} \cdot \bar{w} + \bar{\eta} \cdot \bar{\gamma} \cdot \bar{\psi} \cdot s' \cdot \bar{w} + \bar{\eta} \cdot \bar{\gamma} \cdot \bar{\psi} \cdot \bar{s} \cdot w' + \text{NL}. \end{aligned} \quad (4)$$

Here, a prime indicates the intraseasonal timescale (10–90 days) component, which was subjected to 10–90-day band-pass filtering (Duchon 1979), and an overbar represents the daily climatological mean of factors of the GPI. Thus, the changes in the GPI induced by ISO-related processes and by ISO interaction with the seasonal cycle can be represented by the sum of the five linear terms (with only one perturbation process) and nonlinear effects (with the involvement of two or more perturbation processes, such as $\eta' \cdot \gamma' \cdot \bar{\psi} \cdot \bar{s} \cdot \bar{w}$, $\eta' \cdot \gamma' \cdot \psi' \cdot \bar{s} \cdot \bar{w}$, ..., $\eta' \cdot \gamma' \cdot \psi' \cdot s' \cdot w'$), represented by NL in Eq. (4). The scale-decomposed GPI equation has been used to discuss the effects of ISO on basin-total TC genesis over the eastern Pacific (Jiang et al. 2012) and WNP (Zhao et al. 2015). In this study, we applied this diagnostic method to each of the WNP TC clusters to reveal their formation mechanisms.

3 ISO modulations of seven TC clusters

3.1 Climatological conditions

Figure 2 presents a spectral analysis of the genesis numbers of each TC cluster, as well as all TC cases, over the WNP. Considering that the TC genesis is not a continuous time series and contains several zero values, we utilized the discrete spectrum analysis (Stoica and Moses 2005) to analyze the time series of TC genesis numbers in each summer separately and then displayed their climatological-mean results (Fig. 2). Note that the spectral analysis was not applied to the years without TC geneses (a time series of zero). The results show that, in addition to the synoptic-scale (< 10 days) variability, significant spectral powers associated with the HF and LF intraseasonal variability are seen in the genesis numbers of each cluster. HF and LF ISO correspond

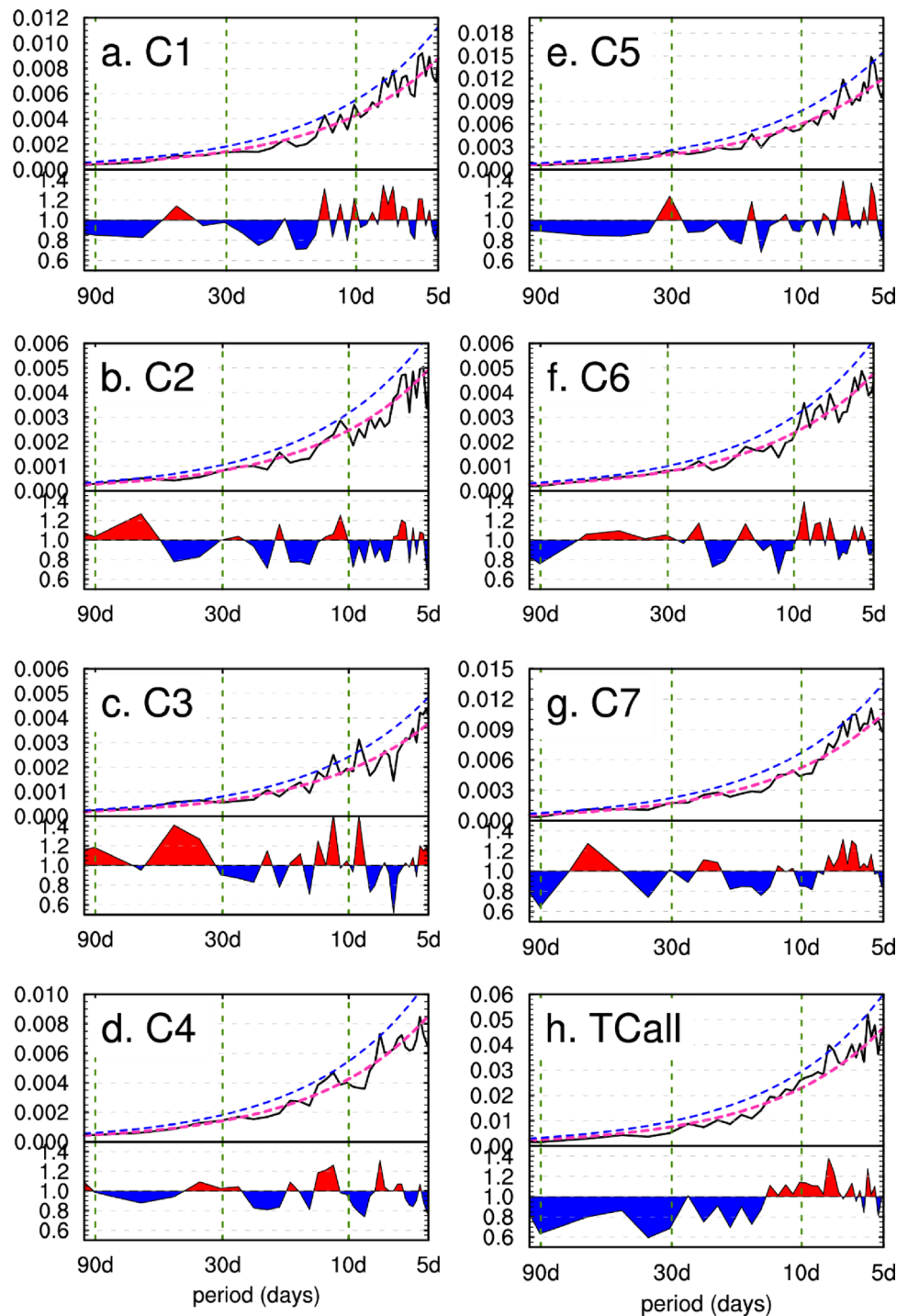
to two dominant ISO modes over the Asia monsoon region. HF ISO is also known as the quasi-biweekly oscillation (QBWO; Keshavamurty 1971, 1972), with a periodicity of 10–30 days, propagating northwestward from the tropics. LF ISO is characterized by a periodicity of 30–90 days (Madden and Julian 1971, 1972) and propagating northeastward. This suggests that TC generations in different locations (in the southeastern part of the WNP for C2–C4 and C6, or near the Philippine Sea for C5 and C7, or within the SCS for C1) are influenced by both HF and LF ISOs.

To confirm the phase relationship between ISO and TC genesis for individual clusters, Figs. 3 and 4 compare the preferred phases of HF and LF ISOs for TC formation. The

evolutions of anomalous convection and circulation associated with HF ISO are displayed in the upper panels of Fig. 3. The convective and low-pressure anomalies are initiated over the western tropical Pacific Ocean in phase 1 (Fig. 3a) and move northwestward towards the eastern Philippine Sea during phases 2–3 (Fig. 3b–c). Then, the convection and low-pressure anomalies become stronger and prevail over the Philippine Sea and SCS in phases 4–5 (Fig. 3d–e), but they weaken after moving into Southeast China during phases 6–8 (Fig. 3f–h). Meanwhile, suppressed convection accompanied by a high-pressure anomaly appears from the western tropical Pacific and moves northwestward toward the SCS (Fig. 3e–h). The statistics of all the WNP TC cases (Fig. 3p) show that about 64% (36%) of all TCs form during periods when the convective (suppressed) anomalies of HF ISO propagate from the western equatorial Pacific towards the SCS during phases 2–5 (6–8 and 1). The contrast in TC genesis numbers between active and inactive phases of HF ISO has been documented previously in Gao and Li (2011), Li and Zhou (2013a), and Zhao et al. (2015). When looking into the phase relationship between HF ISO and the TC genesis numbers of each cluster (Fig. 3i–o), we find that the most favorable (unfavorable) phase for TC genesis varies by cluster type. For example, the TCs of C1 generate the most (least) in phase 4 (phases 8 and 1) when the convective (suppressed) OLR anomalies maximize over the SCS (Fig. 3i). The active convection and low-pressure anomalies extending from the SCS to the Philippine Sea in phases 4–5 also favor the TC formations of C5 (Fig. 3m) and C7 (Fig. 3o). In contrast, the TCs of C4 and C6 tend to generate more frequently in phase 2 (Fig. 3l, and n) when HF ISO convection and low-pressure anomalies are located over the southeastern part of the WNP (Fig. 3b).

Figure 3 indicates that the main genesis locations for the different TC clusters vary according to the convection

Fig. 2 Discrete spectral analysis of daily TC counts of **a–g** individual clusters and **h** all TC cases over the WNP during the TC seasons of 1982–2018 (unit: day^{-2}). The dashed red and blue line represents the significance test of red noise and its 95% confidence level. Red (blue) shading in the lower part of each panel represents the ratio between the spectral power and its red noise when the former is larger (smaller) than the latter, highlighting the significant (non-significant) signals. The spectral analysis was applied to the TC time series each summer respectively and then performed their climatological mean.



and low-pressure anomalies associated with HF ISO. This is also apparent in the phase relationship between LF ISO and the TC genesis numbers of individual clusters (Fig. 4). The zonally elongated OLR and geopotential height anomalies in phase 1 (Fig. 4a) and phase 8 (Fig. 4h) provide favorable conditions for the generation and propagation of the straight-moving clusters C5 and C6, while the opposite conditions appear in phase 5 (Fig. 4m, n). For the TCs

of C3 and C6, i.e., TCs that generate in the southeastern part of the WNP, larger (smaller) numbers of TCs form in phase 1 (phases 4 and 5) when negative (positive) OLR anomalies show a southeastward extension. By comparing the TC genesis numbers against the MJO phase, Camargo et al. (2009) pointed out that the peak genesis numbers for most of the clusters appear in phases 5 and 6 of the MJO (based on the RMM index) as the MJO convection

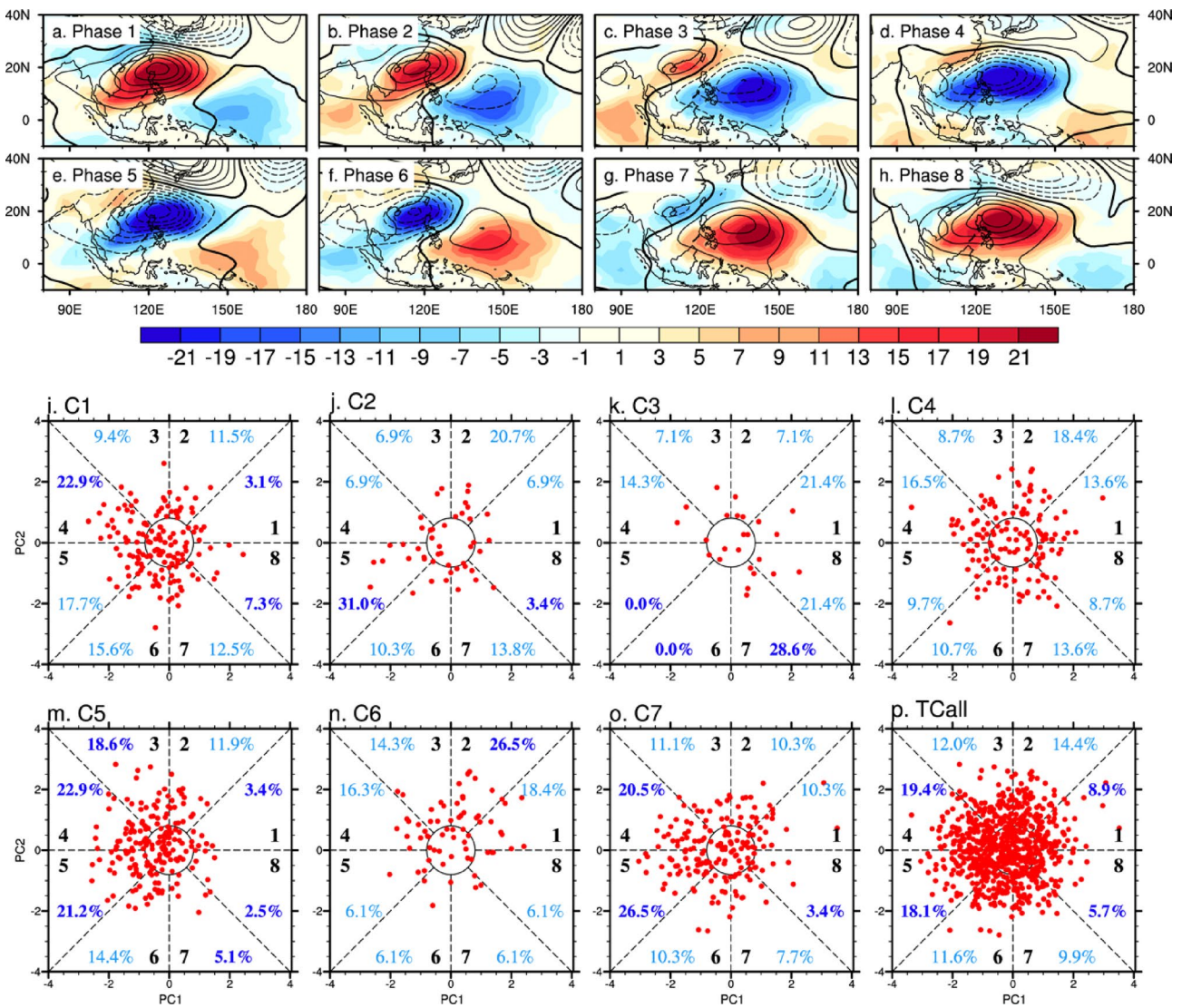


Fig. 3 a–h Composites of 10–30-day OLR (shading; $W m^{-2}$) and 500-hPa geopotential height (contours; interval: 2 gpm) anomalies in the eight phases of active HF ISO [$(PC1^2+PC2^2)^{1/2} \geq 1$]. TC genesis (red dots) of i–o C1–C7 and p TCall during each phase of HF ISO phase indices. The probability of TC genesis in each phase [excluding the days of weak ISO phase, $(PC1^2+PC2^2)^{1/2} < 1$] is shown in blue, where the dark blue number indicates the change in TC genesis counts is statistically significant at the 95% confidence level using the Monte Carlo method. For each TC cluster, each TC genesis date

corresponding to active ISO states (i.e., a specific ISO phase among phases 1–8) is assigned to a random ISO phase, and the probabilities of TC genesis in each phase were then calculated as one simulation. This simulation is repeated a large number of times (1000) to obtain 1000 simulated TC genesis probabilities in each phase. If the observed probability of TC genesis occurrence for a certain ISO phase is larger (smaller) than the 97.5% (2.5%) percentile of the random distribution generated by 1000 simulations, it is considered statistically significant

prevails in the tropical WNP, corresponding to phase 1 in this study.

To understand the modulating effects of ISO large-scale parameters on TC genesis for these distinct clusters, we diagnosed the scale-decomposed GPI (Eq. (4)). Before comparing the contribution of each term to the total GPI, it was necessary to address whether the anomalous GPI can capture the TC genesis for each cluster. Figure 5 shows the composites of HF (10–30-day) and LF (30–90-day) GPI anomalies based on the TC genesis days for each cluster. Both the HF

and LF GPI anomalies reasonably represent the main genesis regions of individual clusters (Fig. 5a–h, i–p). Notably, the HF GPI anomalies have a larger amplitude than the LF GPI for C1, C4, and C6, suggesting a larger contribution of HF ISO to these clusters as shown in the spectral analysis (Fig. 2a, d, f). Even with a smaller amplitude, the GPI anomalies induced by LF ISO capture well the distinct genesis locations for different clusters (Fig. 5i–p). In the analysis of the phase relationship between HF/LH ISO and TC genesis (Figs. 3, 4), we also find that the TCs tend to form

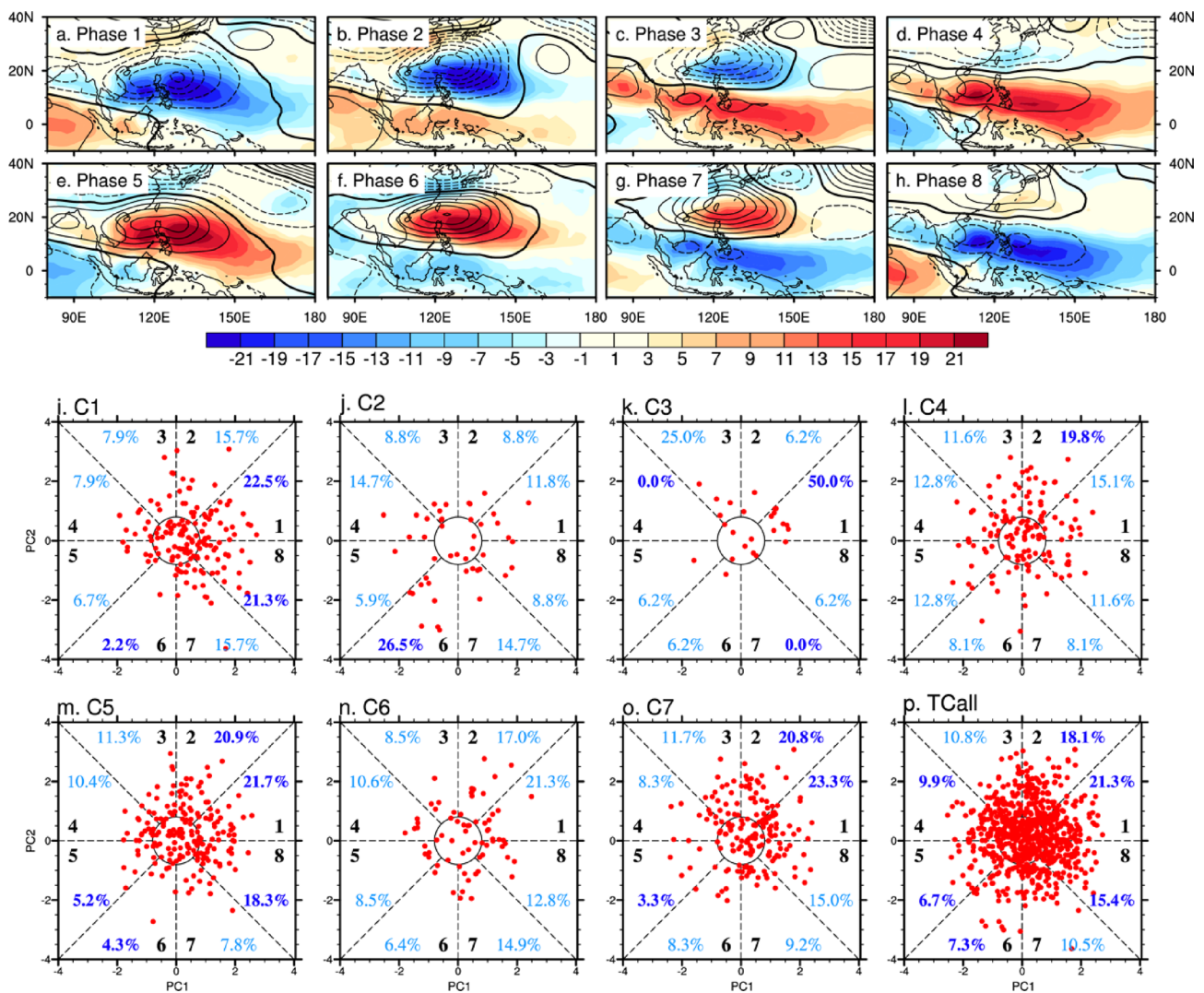


Fig. 4 As in Fig. 3 except for the phase evolution of LF ISO and its association with TC genesis for individual clusters

in the locations with enhanced ISO convection, regardless of 10–30-day or 30–90-day convective signals. For the sake of simplicity, we consider the effects of both ISO modes on the 10–90-day GPI anomalies (Fig. 5q–x). The TCs of various clusters tend to form within the maximum center of 10–90-day GPI anomalies. In other words, the 10–90-day GPI anomalies induced by the combined effect of HF and LF ISO activities could represent the potential of TC genesis for different clusters.

To identify the key processes (dynamic and/or thermodynamic effects) associated with the ISO contributing to the TC genesis of different clusters, we diagnosed and decomposed the GPI for each cluster (Fig. 6). Each term in Eq. (4) was calculated using a $6^\circ \times 6^\circ$ (latitude \times longitude) box centered at each TC genesis location. For all the TC clusters, the relative humidity [$\gamma' = \left(\frac{I_{RH}}{50}\right)^3$] associated with the ISO

plays the leading role in contributing to the 10–90-day GPI anomaly. The low-level absolute vorticity anomaly of the ISO [$\eta' = |10^5 \zeta|^{3/2}$] is the secondary contributor, followed by the effect of ISO-related vertical motion [$w' = \left(\frac{-\omega+0.1}{0.1}\right)$]. The nonlinear effect of ISO–ISO interaction also exerts non-negligible influences on the ISO GPI anomaly, indicating that synoptic-scale activity also feeds back to the ISO (Hsu et al. 2011). In contrast, the effects of ISO-induced potential intensity and vertical wind shear anomalies are relatively small. The results are generally consistent with those of Camargo et al. (2009) and Zhao et al. (2015), who suggested that mid-level relative humidity and low-level absolute vorticity are the two most important factors affecting WNP TC genesis. Note that the results are not sensitive to the size ($3^\circ \times 3^\circ$ or $9^\circ \times 9^\circ$) of the box used for computing the GPI terms.

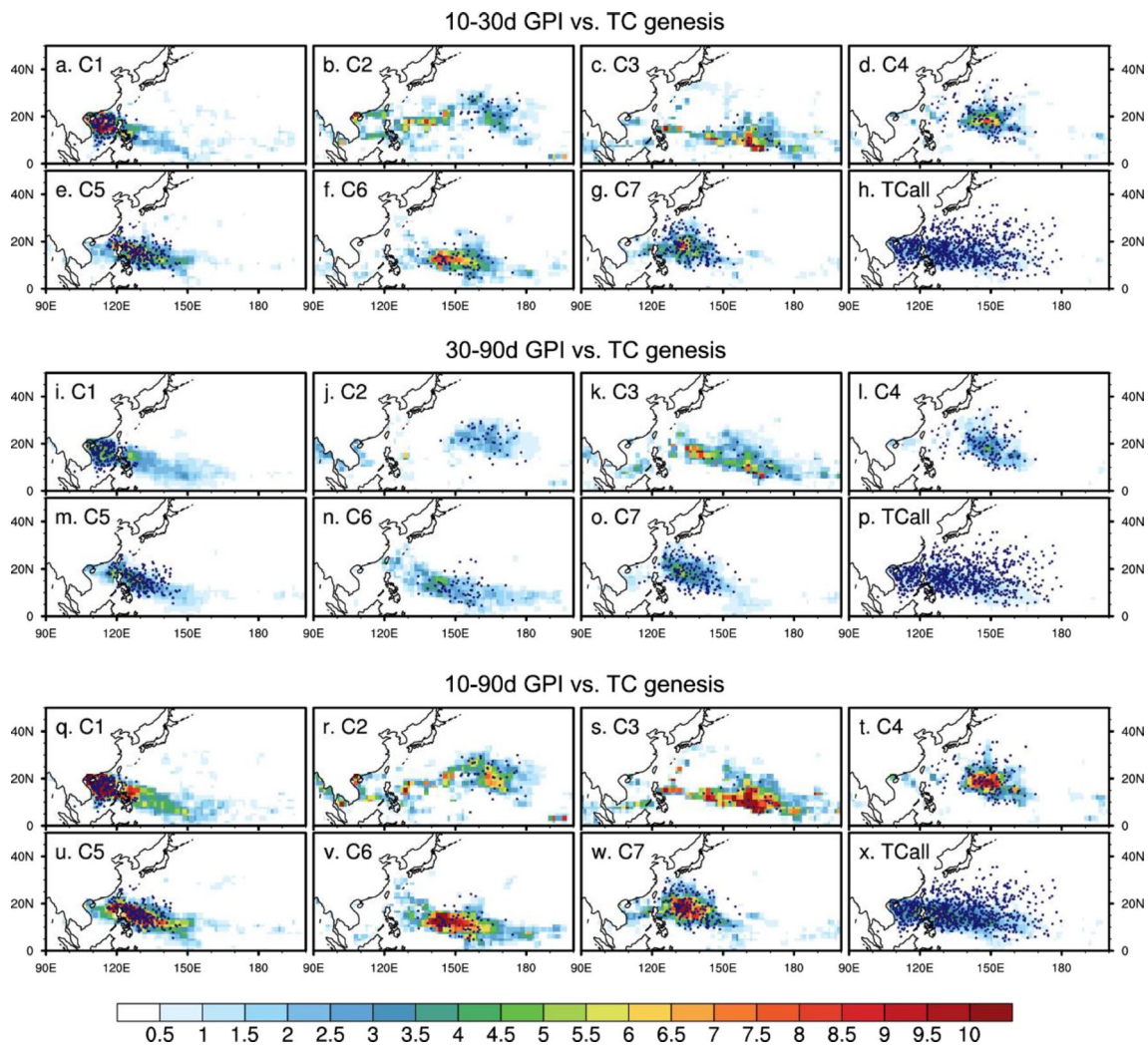


Fig. 5 Composites of HF (10–30-day filtered) GPI anomalies based on TC generation days for (a–g) C1–C7 and (h) TCall during the TC seasons of 1982–2018. i–p and q–x are the same as a–h except for

the LF (30–90-day filtered) and 10–90-day filtered GPI anomalies. Blue dots mark the TC genesis locations

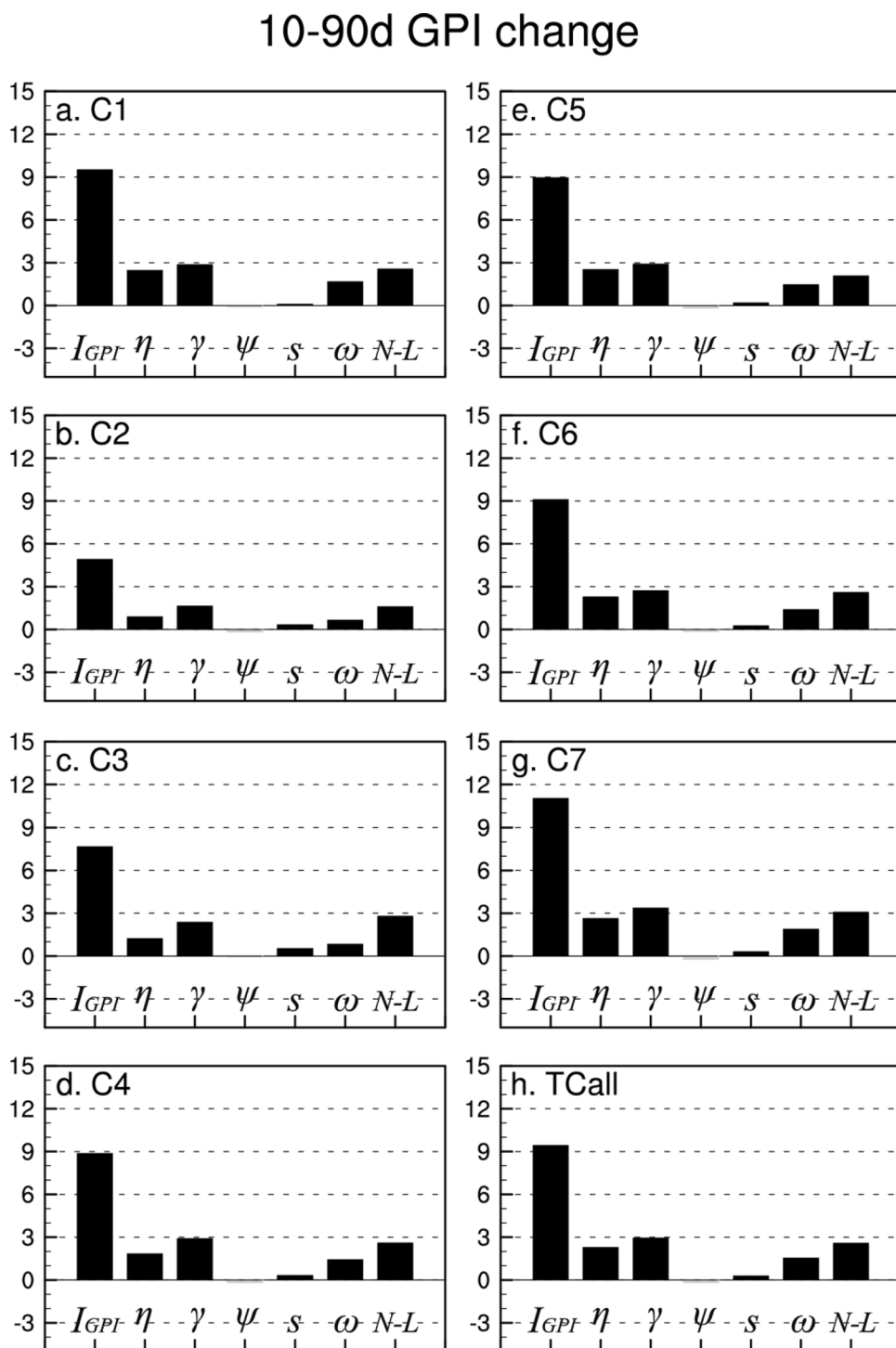
In addition to the influences on TC genesis, the ISO activities may modulate the TC trajectory by changing the background steering flow (Kim et al. 2008; Chen et al. 2009; Li and Zhou 2013b). Figure 7 shows the ISO-related anomalous steering flows (red vectors) in the four days after TC genesis for each cluster. A contrast between straight-moving TCs (C1, C5, and C6) and recurving TCs (C4 and C7) lies in the locations of ISO-related steering flow that regulates the relative intensity and locations of the monsoon trough and subtropical high. Regarding the TCs of C1, the cyclonic steering flow associated with the ISO is confined to the SCS. Concurrently, the WNP subtropical high tends to strengthen and extend westward. The enhanced anomalous southeasterly causes the TCs of C1 to move northwestward (Fig. 7a). A similar condition of a westward extension of the subtropical high together with a weakening of the monsoon trough

can be observed during the TC developing stages of C5 (Fig. 7e) and C6 (Fig. 7f). On the contrary, a northeastward extension of an enhanced monsoon trough, accompanied by weakening trade winds appears after the formation of C4 and C7 TCs (Fig. 7d, g), favoring the northward movement of TCs towards Korea and Japan.

3.2 Compound effects of ISO and ENSO on TCs

The impacts of ENSO on TC activity over the WNP have been investigated and identified as one of the most dominant modes modulating TC activities at interannual time-scales (Wang and Chan 2002; Camargo and Sobel 2005). Nevertheless, the modulations by HF and LF ISOs of the different clusters of TC activities under the various backgrounds of ENSO phases still require further discussion.

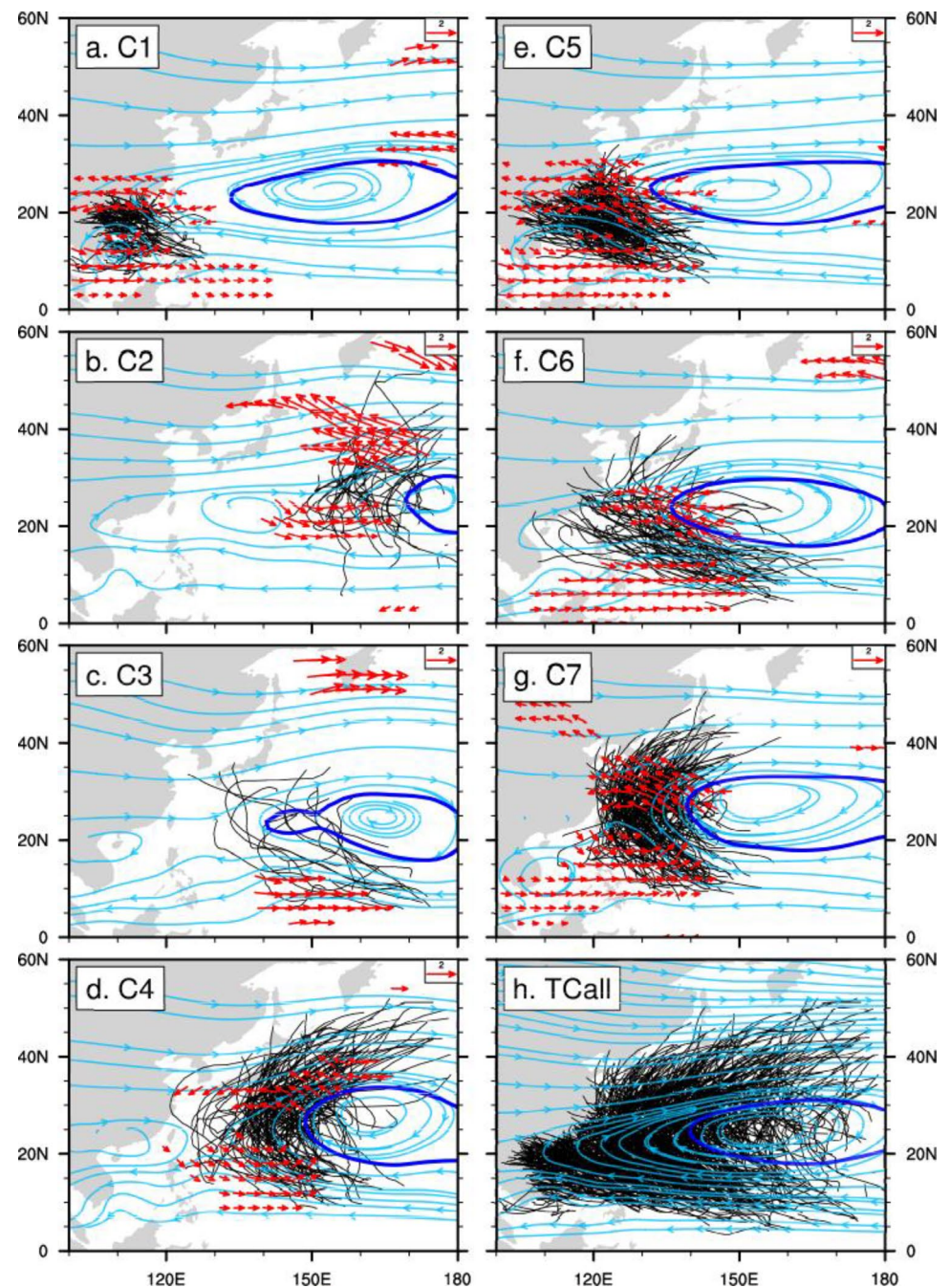
Fig. 6 Contributions of different terms (I_{GPI} , η , γ , ψ , s , ω) to 10–90-day GPI anomalies for **a–g** the TCs of seven clusters and **h** all TCs. These terms are composited over a $6^\circ \times 6^\circ$ box centered at the genesis locations of TCs during the days of TC genesis. Black (grey) bars denote positive (negative) contributions



To assess the modulations of HF/LF ISOs on TC genesis numbers under different ENSO conditions, we calculated the daily TC genesis percentage (TCGP) in each HF/LF ISO phase under different ENSO conditions. The TCGP is defined as the ratio of the TC genesis number relative to the number of days for a particular HF/LF ISO phase. As demonstrated in Fig. 8, the TCGPs of the TCs that generate in the southeast quadrant of the WNP, such as those

of C3, C4, and C6 (Fig. 8c, d, f), indicate greater activity in El Niño years (0.9% TCGP for C3, 2.3% TCGP for C4, and 1.8% TCGP for C6) compared to La Niña years (0.0% TCGP for C3, 1.6% TCGP for C4, and 0.4% for C6). Few TCs of C3 and C6 are generated in La Niña years. Conversely, more landfalling TCs are generated in the western WNP during La Niña years, such as the TCs of C5 (3.0% TCGP in La Niña years and 2.0% TCGP in El Niño years)

Fig. 7 Composites of 10–90-day filtered steering flow (red vectors; unit: m s^{-1}), total (non-filtered) steering flow (light blue streamlines), and the 5880-gpm contour (thick blue contour) based on TC genesis days and the next four days for **a–g** C1–C7. The steering flow in **h** represents the climatological-mean field during the TC seasons of 1982–2018. Steering flow is defined as the pressure-weighted vertically averaged horizontal winds between 850 and 200 hPa. Only the anomalous field exceeding the 95% significance level is shown for the ISO-related steering flow (red vectors). Black curves mark the TC trajectories of **a–g** C1–C7 and **h** TCall



and C7 (2.5% TCGP in La Niña years and 1.8% TCGP in El Niño years).

The different modulations of LF/HF ISOs on the seven TC clusters as well as all TCs over the WNP under El Niño (red bars) and La Niña (blue bars) conditions are shown in Figs. 8a–h/9a–h, respectively. For all TCs over the WNP, the strength of the active convection (depressed convection) over the southeast quadrant of the WNP in phases 1 and 8 (phases 4–5) of the LF ISO is strengthened (offset) by the westerly wind anomalies associated with El Niño conditions (Fig. 8i, k), while it is offset (strengthened) by

the easterly wind anomalies over the southeast quadrant of the WNP with La Niña conditions (Fig. 8m, o). Therefore, a southeast (northwest) shift of positive TCGP anomalies occurs in phases 1 and 8 of El Niño (La Niña) years (Fig. 8i, m) compared to climatological phases 1 and 8 (Fig. 8q). In contrast, the LF ISO-related convection over the WNP in phases 2–3 is essentially strengthened by the enhanced monsoon trough associated with La Niña conditions (Fig. 8n) compared to El Niño years (Fig. 8i), thus resulting in a larger TCGP in phases 2–3 during La Niña years (Fig. 8h).

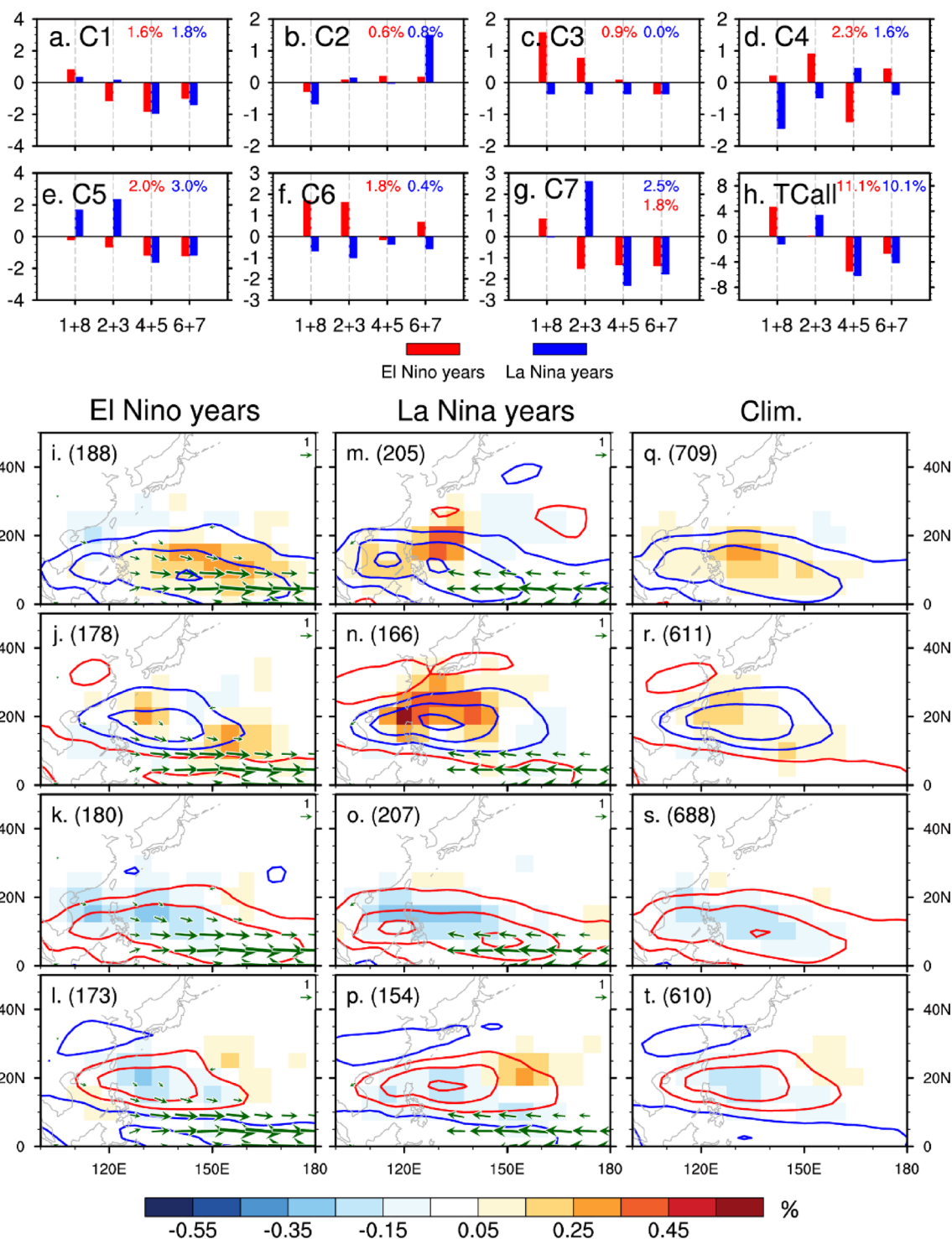


Fig. 8 TC genesis percentage (TCGP) anomalies (units: %) of **a–g** C1–C7 and **h** TCall in each phase of LF ISO in El Niño years (red bars) and La Niña years (blue bars) during 1982–2018. The TCGP of C1–C7 and TCall in El Niño (numbers in red) and La Niña (numbers in blue) years are displayed in the right-top corner of the subplots. **i–k** Composite TCGP (shading; units: %) anomalies and 30–90-day bandpassed OLR anomalies (contours from -20 W m^{-2} to 20 W m^{-2} with an interval of 8 W m^{-2} , positive and negative values are in red and blue contours, respectively) in **i, m, q** phases 1 and 8, **j, n, r** phases 2–3, **k, o, s** phases 4–5, and **l, p, t** phases 6–7 of LF ISO during **i–l** El

Niño, **m–p** La Niña, and **q–t** all years. The green vectors in **i–t** represent the climatological wind at 850 hPa composited in **i–l** El Niño years, **m–p** La Niña years, and **q–t** all years during 1982–2018. Only the regions with significant changes at the 95% confidence level are shown. TCGP anomalies are defined as the percentage of TC genesis count divided by the number of days for each phase of LF ISO and El Niño (La Niña) years compared with the climatological mean for each $5^\circ \times 5^\circ$ grid box. The number of days for each phase of LF ISO and El Niño (La Niña) years is listed in parentheses

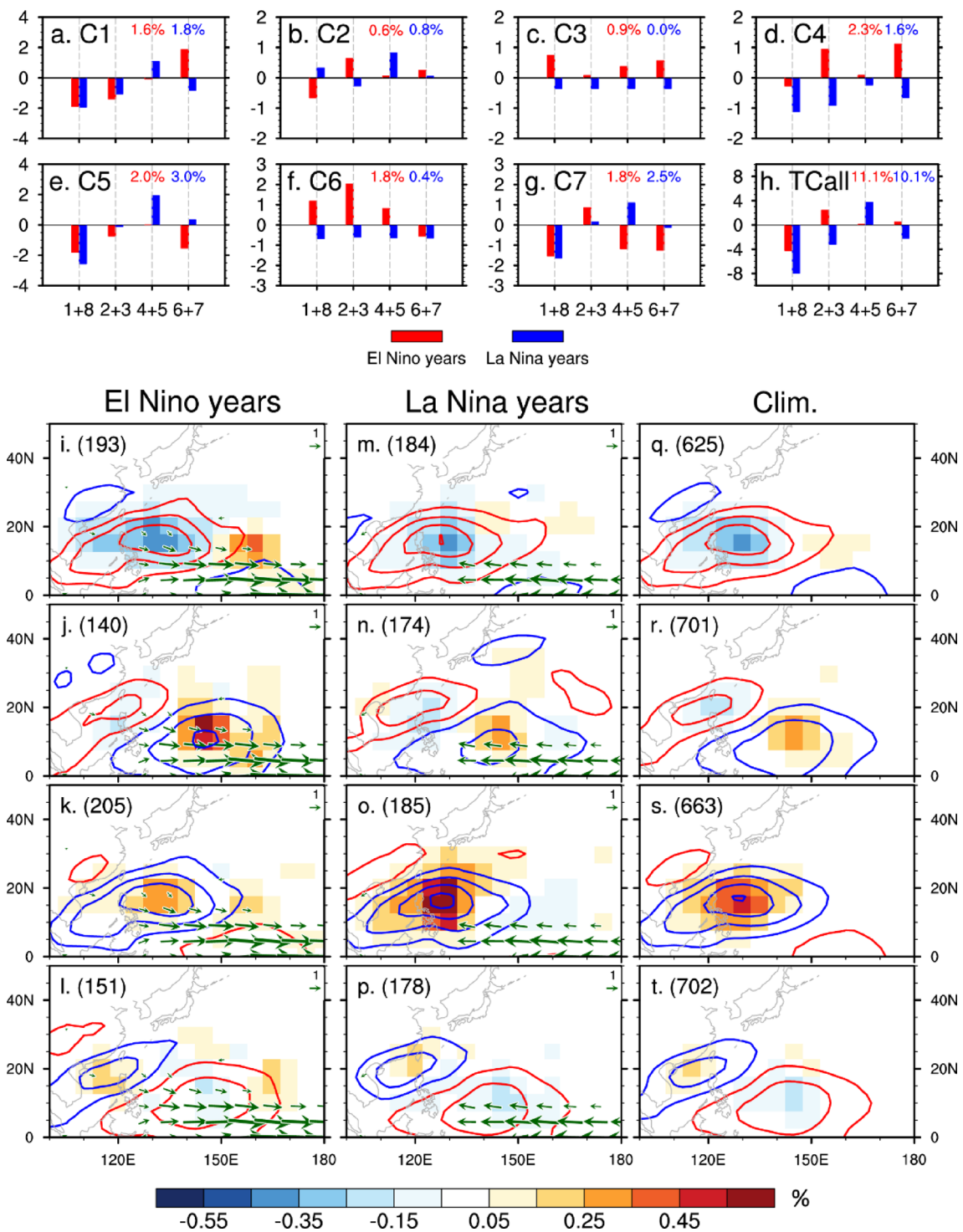


Fig. 9 As in Fig. 8 except for TC count anomalies and large-scale fields in each phase of HF ISO

The HF ISO and ENSO also impact TC activities by changing the low-level winds associated with El Niño and La Niña years. The convections in the southeast quadrant of the WNP associated with phases 2–3 of HF ISO are enhanced (offset) by the westerly (easterly) anomalies

associated with El Niño (La Niña) conditions (Fig. 9j, n). Furthermore, the modulation of ISO has different impacts on different TC clusters in El Niño and La Niña years. For the TCs of C3 and C6 generated in the southeast quadrant of the WNP, the TC genesis number anomalies of these clusters

are negative in almost all phases of LF (blue bars in Fig. 8c, d, f) and HF (blue bars in Fig. 9c, d, f) ISO during La Niña years, indicating a weaker modulation of ISO in La Niña years for these two clusters compared with those in El Niño years. Strong easterly (westerly) anomalies over the tropical WNP associated with La Niña (El Niño) conditions suppress (enhance) the TC genesis numbers in the southeast quadrant of the WNP. In contrast, the TC genesis number anomalies of landfalling TCs, such as the TCs of C5 and C7, are negative in most phases (at least six out of eight phases) of LF (Fig. 8e, g) and HF (Fig. 9e, g) ISO during El Niño years, which results from the southeasterly steering flow of landfalling TCs being offset by the westerly anomalies associated with El Niño conditions. Moreover, the composite results in Figs. 8 and 9 are not sensitive to the threshold of Niño-3.4 SST anomaly (0.8σ) used. For example, the larger threshold of 1.0σ and smaller threshold of 0.7σ are nearly identical (not shown).

In summary, we have examined the influences of ISO on the activities of individual TC clusters in this section. Our findings indicate that the location of TC genesis varies with the convective and low-pressure anomalies of both the HF and LF ISO modes. We have identified mid-tropospheric moistening and low-level cyclonic vorticity associated with ISO as being the leading contributors to TC genesis for all seven clusters. While El Niño and La Niña have similar impacts on TC genesis in most phases of LF and HF ISO, the modulation of LF and HF ISOs in some specific phases is still changed by the low-level winds associated with ENSO conditions. Additionally, we observed relatively weaker modulations of HF and LF ISOs on the TCs generated in the southeast quadrant of the WNP (landfalling TCs), such as the TCs of C3, C4, and C6 (C5 and C7), during La Niña (El Niño) years compared with those in El Niño (La Niña) years. These observations provide a physical basis for predicting the TC genesis numbers of each cluster using ISO-related fields as predictors. Given that each TC cluster has a distinct genesis location and trajectory, once the genesis numbers of individual clusters are predicted, the probability of TCF over the entire WNP basin can be obtained by integrating the track patterns for all clusters. Next, we provide a detailed description of the statistical prediction model and assess the WNP TC prediction skill at the subseasonal timescale.

4 Application to subseasonal TC prediction

4.1 Construction of statistical model

The modulation by ISO and ENSO of the TC genesis of each cluster (Figs. 2, 3, 4, 5, 6, 7, 8, 9) provides a source of predictability for TC genesis at the subseasonal timescale. Then, by combining the TC track density of the seven clusters, we can

obtain a probability map of TCF. This prediction method was proposed by Camargo et al. (2007a) and applied to predicting seasonal TCs by Chu et al. (2010) and Kim et al. (2012). In this study, we developed a statistical model to predict the TC genesis numbers and the probability distribution of TC tracks in every 10-day period at forecast lead times of 10–40 days.

Figure 10 illustrates the detailed steps of the prediction model's construction. The first step is to obtain distinct TC clusters by applying the clustering method to the historical (1982–2008) TC best-track dataset (such as the result in Fig. 1). Since the TCs rarely occurred in a daily interval, our predictand here is the TC count in every 10-day period to pay more close attention on the intraseasonal variations of TC activity. Considering that the seasonal cycle of TC count is steady climatologically, we focus only on the prediction of TC count anomalies (deviations from a seasonal cycle of 10-day means). The seasonal cycle 10-day mean for each TC cluster retains only the mean and the first three harmonics of the daily climatology (black curves in Fig. 11) during the training period (1982–2008). Considering the different modulations of ISO under different ENSO phases, we constructed different statistical models for different ENSO phases. In other words, three statistical models were developed for each TC cluster: one for El Niño years, one for La Niña years, and another for neutral years. Thus, in the second step, based on the lead–lag relationships between TCs and ISO anomalies with a temporal resolution of a 10-day period (10-day mean), the potential predictors associated with ISO environments (mainly the factors of GPI and SST) are selected. Then, a linear regression model is derived for predicting anomalous TC numbers of each cluster in different ENSO phases.

Using the preceding ISO-related predictors, the anomalous TC counts of individual clusters in different ENSO phases are predicted. By adding the climatological seasonal cycle of 10-day period TC counts to the predicted anomalies of TC counts, the total TC counts for each cluster can be obtained. The final step (Step 3 in Fig. 10) is to construct the probability maps of TCF over the entire WNP basin. The TCF is defined as the frequency of TC occurrence in a particular $5^\circ \times 5^\circ$ (latitude \times longitude) grid box, which indicates how often TCs pass through a specific grid box. This could be achieved by multiplying the TC counts of each cluster by the climatological probability of the track density of the corresponding ENSO phases. The results of all seven clusters are then summed. Following Kim et al. (2012), the TCF probability formula can be written as:

$$P_{k,m}^{\text{obs}}(\text{lat}, \text{lon}) = \frac{\text{Freq}_{k,m}^{\text{obs}}(\text{lat}, \text{lon})}{N_{k,m}^{\text{obs}}} \times 100\%, \quad (5)$$

where the variables with the superscript “obs” are observed variables in the m th 10-day period of the k th year; “lat” and

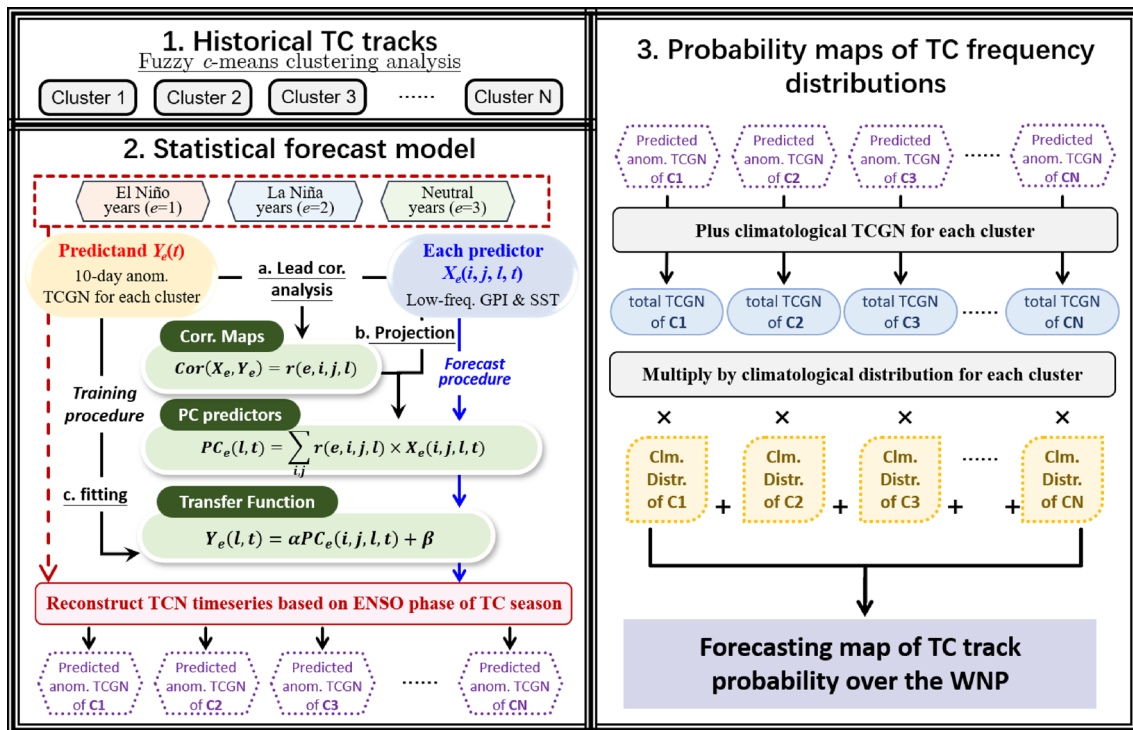


Fig. 10 Steps for constructing the subseasonal TC prediction model

“lon” are the latitude and longitude in degrees, respectively; $Freq_{k,m}^{obs}(lat, lon)$ indicates the observed TCF within 5° of a grid point (lon, lat); and $N_{k,m}^{obs}$ is the observed total TC count over the entire WNP. Note that the TCF probability may exceed 100% when TCF is larger than TCN. For instance, if only one TC is observed over the WNP basin (TCN = 1), but it remains consistently over a specific grid box for 12 h (TCF = 2). The TCF probability equals to 200%.

A predicted probability map of TCF [$P_{k,m}^{fcst}(lat, lon)$] can be approximately equal to the sum of the seven clusters of the climatological probability of corresponding ENSO phases multiplied by the predicted TC counts (anomalous counts plus climatological 10-day period TC counts):

$$P_{k,m}^{fcst}(lat, lon) = \frac{1}{N_{k,m}^{fcst}} \left[\sum_{n=1}^N N_{C_n,k,m}^{fcst} \times \bar{P}_{e,C_n,m}^{obs}(lat, lon) \right] \times 100\%; \tag{6}$$

$$\bar{P}_{e,C_n,m}^{obs}(lat, lon) = \sum_{k=1}^K \frac{Freq_{e,C_n,t,l}^{obs}(lat, lon)}{N_{e,C_n,t,m}^{obs}}. \tag{7}$$

Here, the variables with the superscript “fcst” are the predicted variables; C_n represents the n th cluster; N is the total number of clusters (i.e., seven in this study); $\bar{P}_{e,C_n,m}^{obs}(lat, lon)$ is the m th climatological probability of C_n during K years; and e is the ENSO phase of a specific TC season ($e = 1, 2, 3$

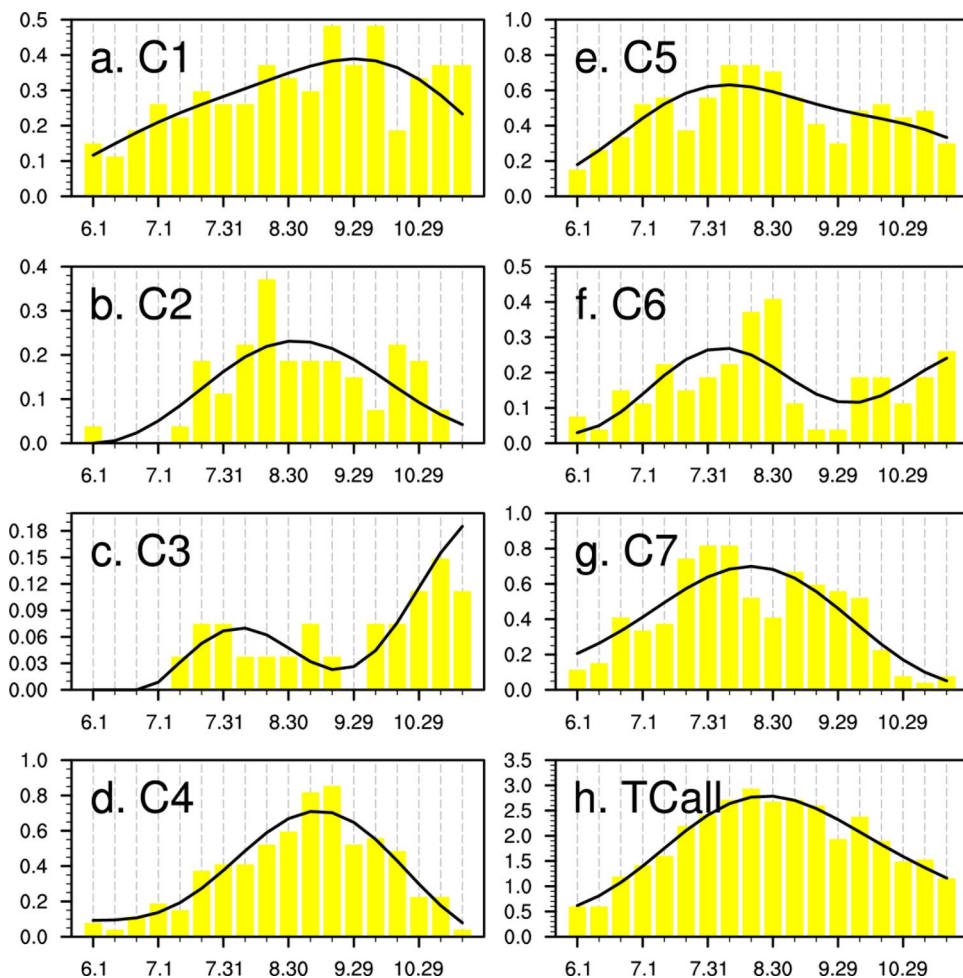
refers to El Niño, La Niña, and neutral years, respectively). Here, the climatological probability is calculated using the TC data during the training period (1982–2008).

A “perfect reconstruction” based on “true” TC counts (instead of predicted TC counts) is used as the assessment benchmark. The perfect reconstruction probability [$P_{k,m}^{pfrc}(lat, lon)$] is written as

$$P_{k,m}^{pfrc}(lat, lon) = \frac{1}{N_{k,m}^{obs}} \left[\sum_{n=1}^N N_{C_n,k,m}^{obs} \times \bar{P}_{C_n,m}^{obs}(lat, lon) \right] \times 100\%. \tag{8}$$

We use the first 27-year period (1982–2008) as the training period and the last 10-year period (2009–2018) as the independent forecast period. During a TC season, there are 18 10-day-mean time points (1–10 June, 11–20 June, ..., 18–27 November). Thus, we include 486 10-day time points (18 10-day-mean time points \times 27 years) in the training period and 180 10-day-mean time points (18 10-day-mean time points \times 10 years) in the forecast period. For a real-time operational application, the ISO (10–90-day) components are derived using a non-bandpass filtering method (Hsu et al. 2015). The following two steps are performed. First, the daily anomaly fields are obtained by subtracting the climatological mean and the first three harmonics of the climatological annual variability from the raw data to remove the low-frequency background state. Then, a 10-day mean

Fig. 11 Climatological 10-day mean TC counts of **a–g** C1–C7 and **h** TCall. The yellow bars and thick black lines are the raw climatology and the smoothed annual cycle (only the mean and first three harmonics of the daily climatology retained) of the years 1982–2008



is applied to match the prediction interval of a 10-day mean and to remove the synoptic-scale component (with a period shorter than 10 days).

4.2 Selection of predictors

To identify potential predictors for each TC cluster, we analyze a lead–lag correlation analysis between anomalous TC counts and preceding ISO-related dynamic and thermodynamic factors, including the GPI and its associated parameters in different ENSO phases (Fig. 12). For instance, if the preceding MPI (Emanuel 1995) anomalies, which encompass the influences of oceanic and atmospheric thermodynamic factors like SST and vertical profiles of air temperature and specific humidity, exhibit a notable correlation with the genesis of a particular TC cluster, we can consider them as potential predictors for forecasting this type of TC.

The results show that the TC genesis counts are not only correlated with local environmental conditions during the genesis period (lead 0d; top panels), but also with remote effects associated with the spatiotemporal evolution of the ISO (lead 10–40d, shown in seven lower panels).

Moreover, significant correlation patterns between TCs and ISO-related dynamic and thermodynamic factors vary in different ENSO conditions (Fig. 12b–d, f–h). Although the predictors are selected based on the statistically significant grid points, the correlation patterns are large in scale. For instance, the anomalous TC counts of C1 are positively correlated with GPI anomalies in the main genesis regions situated over the tropical WNP (Fig. 12a1). This positive GPI anomaly emerges in the tropical WNP about 20 days before TC genesis (Fig. 12a4) and then propagates northeastward towards the western WNP region (Fig. 12a1–a4). Additionally, the anomalous TC counts of C6 are positively correlated with MPI anomalies over the eastern Pacific and negatively correlated with MPI anomalies over the western Pacific, as in the El Niño condition in the climatology (Fig. 12e). This finding suggests that ISO-related SST anomalies, like the El Niño-related large-scale pattern, could modulate the TC genesis frequency on the ISO timescale. The correlation maps between ISO-related dynamic and thermodynamic factors during positive and negative ENSO phases demonstrate the intraseasonal correlations between anomalous TC counts and the preceding

TCC of C1 & GPI

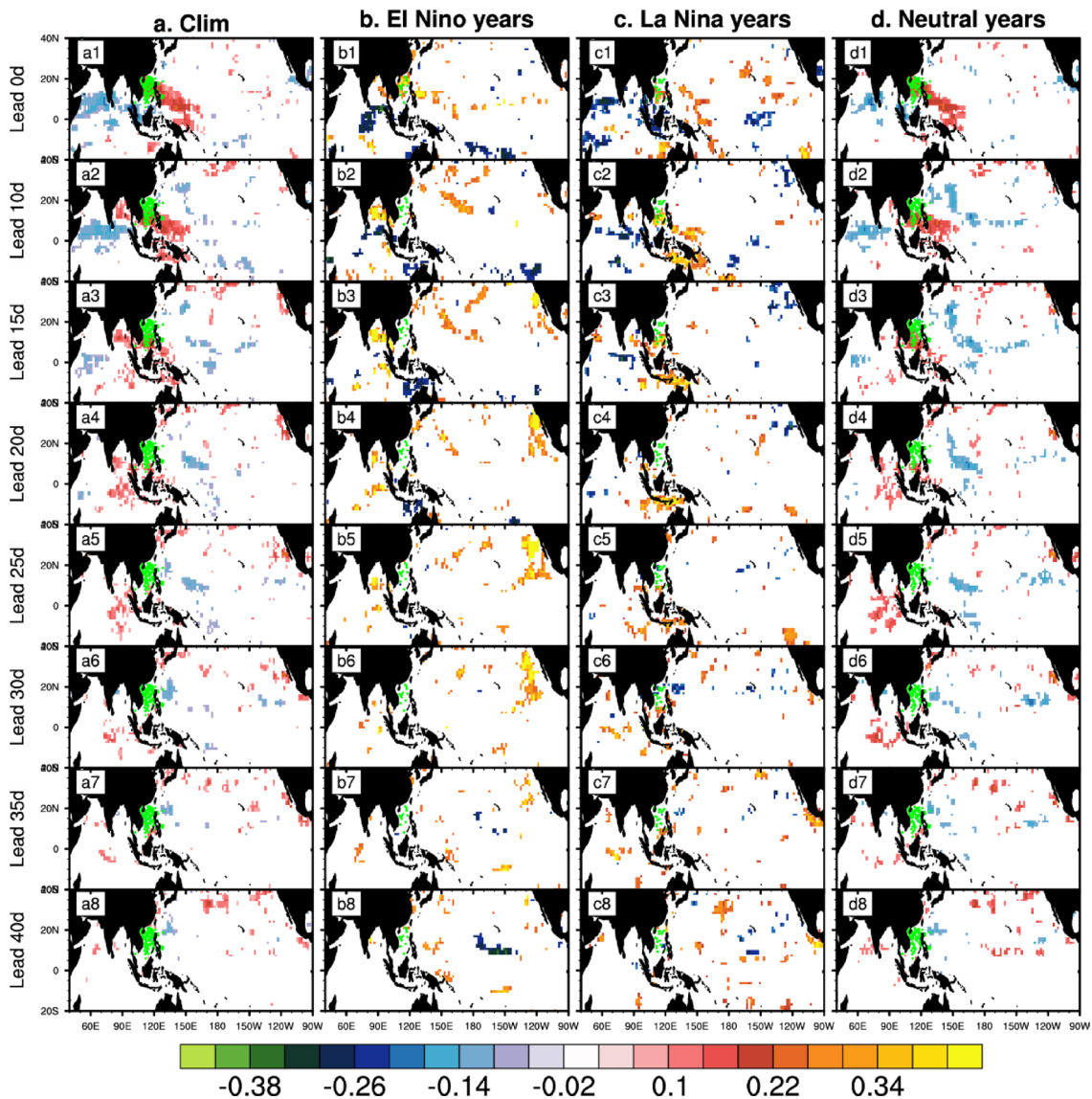


Fig. 12 Temporal correlation coefficients (TCCs; shading) between TC count anomalies of **a–d** C1 and GPI, and **e–h** C6 and MPI during **a, e** all years, **b, f** El Niño years, **c, g** La Niña years, and **d, h** neutral years of 1982–2008, at 0-day, 10-day, 15-day, 20-day, 25-day, 30-day,

35-day and 40-day leads (from top to bottom). Only the TCCs that are statistically significant at the 95% confidence level are shown. TC genesis locations are represented as green dots

ISO-related factors, which exclude the low-frequency influence of ENSO. For example, compared to the climatological correlations, the positive MPI anomalies over the central and eastern Pacific disappear and only negative MPI anomalies are found over the tropical central Pacific during El Niño years (Fig. 12e). The climatological negative MPI anomalies over the tropical WNP become positive and disorganized (Fig. 12b). In contrast to El Niño years, negative and positive MPI anomalies are found over the tropical WNP and eastern North Pacific, respectively, during La Niña years (Fig. 12c).

Considering the different correlation patterns between anomalous TC counts and ISO-related large-scale fields in different ENSO phases and the spatiotemporal evolution of the ISO (e.g., Fig. 12), it is cumbersome and subjective to select predictors based on the highly correlated box for each ENSO phase, each forecast lead time, and each cluster. Therefore, we use a method similar to STPM in Hsu et al. (2015) to select predictors. First, in terms of the correlation coefficient (Cor) patterns for regions where anomalous TC counts (X_i) for each cluster and the ISO-related large-scale fields (Y_j) are statistically significantly correlated at the 95%

TCC of C6 & MPI

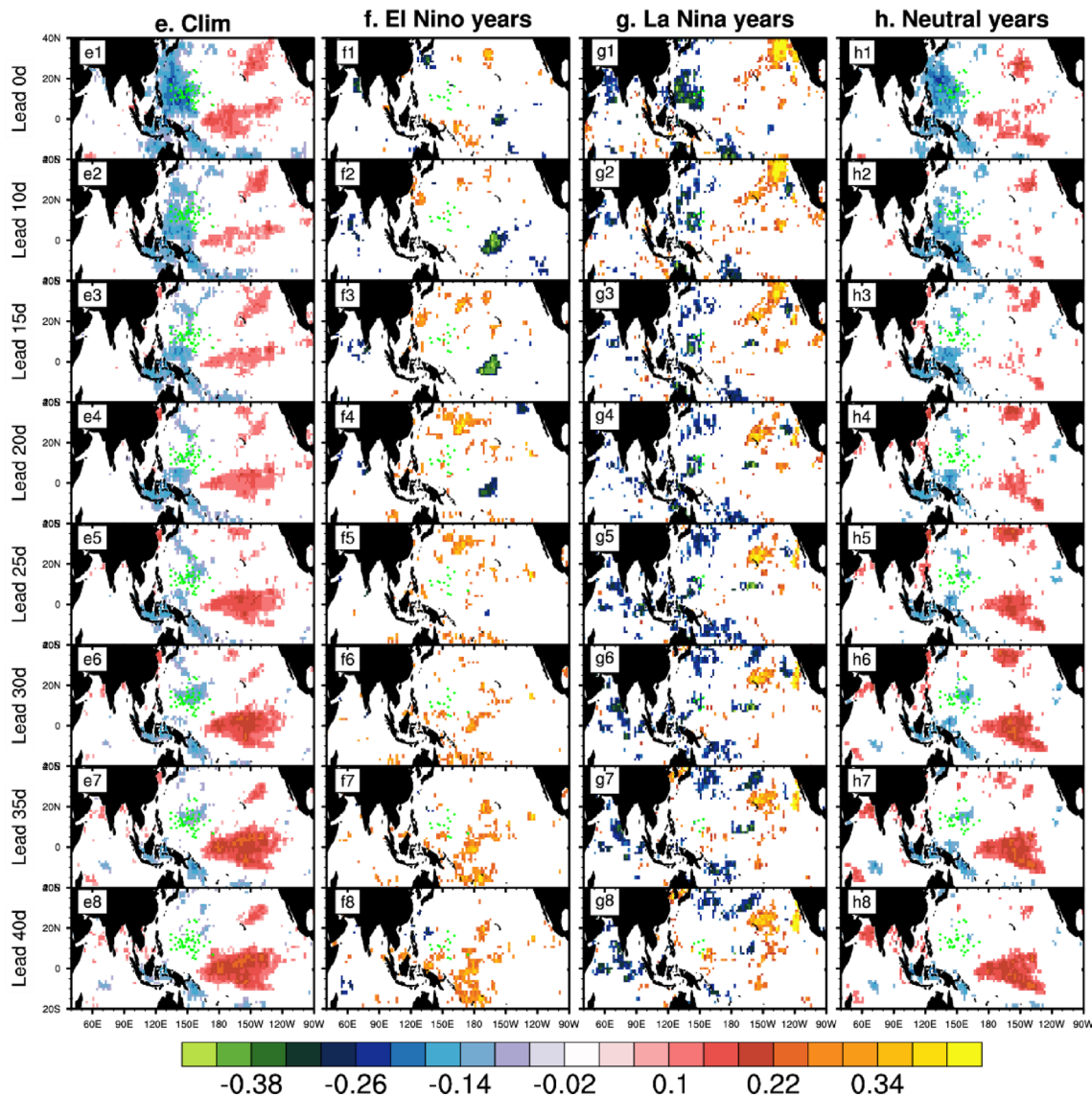


Fig. 12 (continued)

confidence level (i.e., shading in Fig. 12), we focus only on those over Asia and the North Pacific (20° S–40° N, 40° E–90° W):

$$\text{Cor}(X_e, Y_e) = r(e, i, j, l), \tag{9}$$

where i and j denote the zonal and meridional grid points, respectively, l represents the lead times for the prediction time, and e indicates the ENSO phases of the TC seasons (i.e., Figs. 12b–c, f–h). Next, the PC predictors associated with large-scale fields are obtained by projecting anomalous large-scale fields onto $\text{Cor}(X_e, Y_e)$ fields. The transfer function is then constructed by using a linear regression method.

The parameters α and β are the regression coefficients of the prediction model during the training period. For each TC cluster, there are seven statistical models (seven predictors) for each ENSO phase.

When we start the forecasting procedure, the ENSO phase of the TC season is first predicted based on the NMME prediction results. The predicted ENSO phase of the TC season determines which statistical model we choose. For example, if the Niño-3.4 index exceeds 0.8σ , we choose the El Niño statistical model ($e = 1$) to predict each TC cluster. Note that the NMME has stable and skillful predictions for ENSO conditions. Temporal correlation coefficients between the observed and predicted Niño-3.4 index for TC seasons at

1- to 3-month lead forecasts range from 0.94 to 0.97, which are statistically significant at the 99% confidence level. Despite decreasing model skill with longer lead times, correlation coefficients remain significant even for the 9-month lead forecast. Proficiently predicting ENSO state months provides us with the assurance to employ suitable statistical models for TC predictions based on both HF and LF signals.

4.3 Prediction skill of subseasonal TC activity

Figure 13 depicts the overall prediction skill of the statistical model based on the assessments of independent forecast results. The figure represents the temporal correlation coefficient (TCC) and root-mean-square error (RMSE) associated with each predictor at various lead times. As shown in Fig. 13, the model's prediction skill tends to diminish as the lead time increases, as evidenced by smaller TCCs and larger RMSEs. Notably, for the prediction of anomalous TC counts, the TCCs and RMSEs associated with TCall (Fig. 13a) and the sum of C1–C7 (Fig. 13b) differ among predictors at lead times of 15–30 days. Specifically, the RMSE of TCall ranges from 1.0 to 1.3, while that of the sum of C1–C7 increases to 1.1–1.75. Furthermore, the vertical velocity at 500 hPa exhibits the highest prediction skill for both TCC and RMSE among six predictions (gray lines in Fig. 13), whereas the GPI shows the fastest drop in prediction skill (red lines in Fig. 13). Although the SSTA predictor does not demonstrate the highest prediction skill during lead 0–10 days, its prediction skill remains stable even at lead times beyond 25 days (pink lines in Fig. 13). Additionally,

the ensemble prediction's TCC is statistically significant at the 95% confidence level at a lead time of 30 days (thick black lines in Fig. 13).

To demonstrate the importance of developing statistical forecast models tailored to different ENSO conditions, we compared our statistical model that incorporates ENSO effects (red lines, hereafter referred to as ENSO-fcst) with a simple statistical model based on climatological correlations that do not consider ENSO effects (blue lines, hereafter referred to as clim-fcst), as depicted in Fig. 14a. The analysis reveals that the prediction skills of ENSO-fcst and clim-fcst models are comparable at lead times of 10–15 days. However, at lead times of 20–40 days, the TCCs of the clim-fcst forecast model decline more rapidly and become statistically insignificant at the 95% confidence level, whereas the TCCs of the ENSO-fcst forecast model decrease more gradually and retain prediction skill up to a lead time of 30 days. The superior TCCs of the ENSO-fcst forecast model over the clim-fcst model indicate the advantage of developing statistical models that account for different ENSO phases. Furthermore, we observe that for the prediction of anomalous TC counts, the prediction skill of the sum of C1–C7 is higher than that of TCall at lead times of 10–30 days, indicating the need to construct statistical forecast models for individual TC clusters. We also utilized a stepwise multiple linear regression model to predict anomalous counts for each cluster at each lead time (not shown). The prediction skills were less skillful than that of the ensemble mean of linear regression models by each predictor. This may be attributable to the persistence of overfitting in the multiple linear regression.

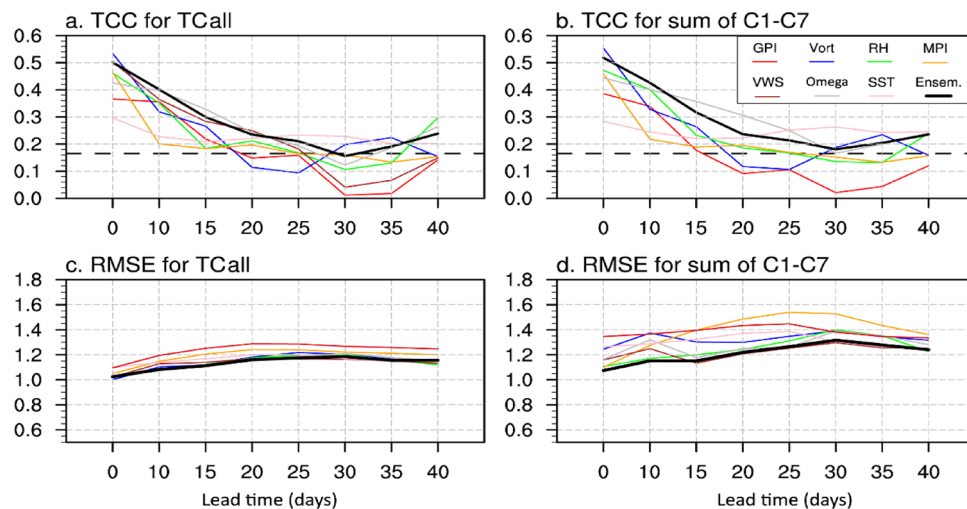


Fig. 13 **a** TCCs and **c** RMSEs between observed and predicted TCall count anomalies. **b**, **d** As in **a**, **c** but for the sum of C1–C7. Red, blue, green, orange, brown, gray, and pink lines in **a–d** denote the forecast skills by using GPI, GPI components associated with vorticity at 850 hPa (Vort), relative humidity at 700 hPa (RH), MPI, the vertical wind

shear (WVS), the vertical velocity at 500 hPa (Omega), and SST as predictors, respectively. Thick black lines represent the skills of the ensemble results. Dashed lines in **a–b** mark the 95% confidence level of the Spearman rank order correlation coefficients based on the effective degree of freedom

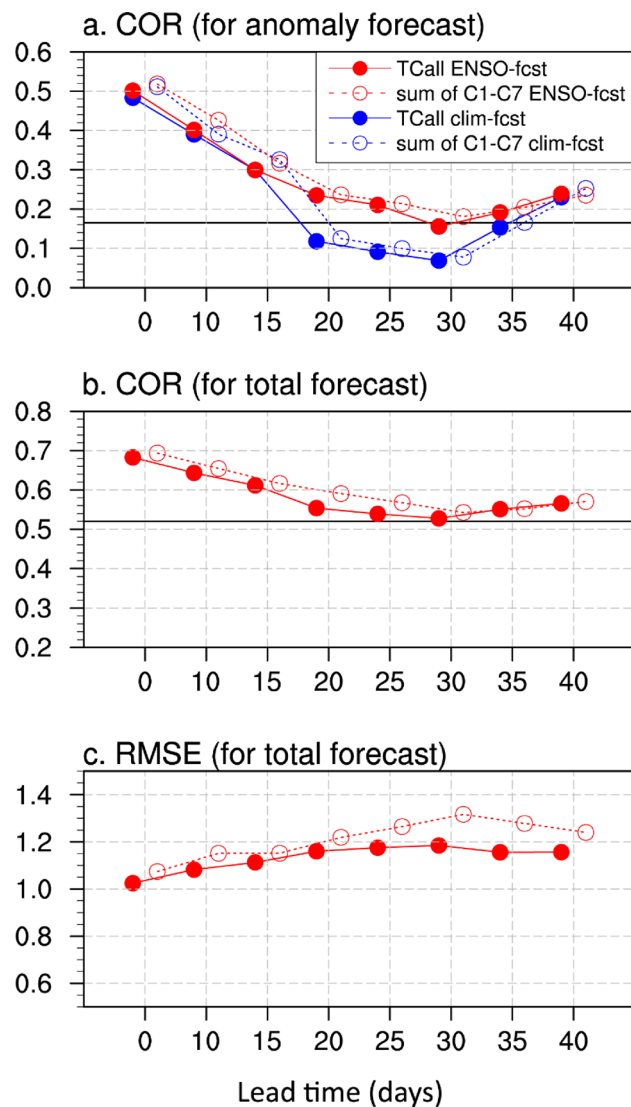


Fig. 14 TCCs between the observed and predicted **a** anomalous and **b** total TC count (sum of C1–C7 in blue, TCall in red) and **c** the RMSEs of total TC counts (open dot-dashed lines indicate the results of the sum of C1–C7; solid dot lines indicate the results of TCall) at different forecast lead times from 0 to 40 days (x -axis). The black line in **a** is the 95% significance level of the Spearman rank order correlation coefficient based on the effective degree of freedom. The black line in **b** is the TCC skill of climatological prediction. Blue dotted lines represent the TCC prediction skill of clim-fcst statistical models

After adding the climatological 10-day-mean TC counts to the predicted TC count anomalies, the TCCs of the sum of C1–C7 at the lead times of 10–30 days are higher than the climatological prediction, but they are lower than the climatological prediction after the 30-day forecast lead (Fig. 14b). The climatological prediction is the result of climatological 10-day-mean TC counts during the training period. The RMSEs are standard deviations of 1.00–1.35 (Fig. 14c). The reason why we utilize the intraseasonal anomaly deviations from the seasonal climatology as predictands in a linear

regression model instead of total TC counts as predictands in a Poisson regression model is that the significant seasonal climatology of TC counts would contribute most of the prediction skill in a total TC counts prediction model. We also developed a Poisson regression model for the total TC counts by utilizing the same potential predictors as described in Sect. 4.2. The prediction skill of the Poisson regression model was at a lead time of 10 days (not shown), which is lower than the result of the current linear regression model. Once the TC counts for each cluster are predicted, the probability map of TCF can be obtained by considering the climatological TCF distribution (introduced in Sect. 4.1). Here, we show four TCF cases to provide a visual impression of TCF prediction (Fig. 15). Four TCF cases are during 21–30 June 2012, 10–19 August 2018, 31 July–9 August 2014, and 9–18 September 2010. The model can predict the regions with a higher probability of TCF in the observation (top panels in Fig. 15) at the lead time of 10–20 days. The predicted probability map of TCF of the perfect construction (second from top panels in Fig. 15) reveals errors of the model predicted biases in TC counts for a specific cluster (or some clusters).

5 Discussion and conclusions

Although ISO and ENSO modulations of basin-wide TC activities have been documented (Chia and Ropelewski 2002; Wang and Chan 2002; Camargo et al. 2007a; Li and Zhou 2013a, b; Zhao et al. 2015), how the 10–30-day and 30–90-day ISOs influence distinct TC clusters (with different genesis locations and trajectories) over the WNP and the ENSO effects on ISO–TC connection needed further examination, as addressed in this study. Specifically, we classified the WNP TCs into seven clusters using the fuzzy c -means clustering method (Fig. 1), consistent with previous studies (Camargo et al. 2007a, b; Kim et al. 2011; Zhang et al. 2016b; Qian et al. 2020). Based on a spectral analysis of TC genesis counts for each cluster, it was found that all seven clusters display significant variability at subseasonal timescales, with peak spectrums in the HF (10–30-day) and LF (30–90-day) ISO bands (Fig. 2). The probability of TC genesis for each cluster varies with the phase evolutions of the two ISO modes (Figs. 3, 4). Generally, the TCs of each cluster are more likely to be generated when the ISO convective and low-pressure anomalies propagate into the main genesis regions of the specific cluster (Figs. 3, 4).

To elucidate the modulating effects of the two ISO modes on the genesis of different clusters of TCs, the scale-decomposed GPI anomalies were diagnosed (Fig. 6), because the intraseasonal GPI distribution can capture the genesis patterns of individual clusters (Fig. 5). The diagnostic results suggest that the ISO-related relative humidity is the leading

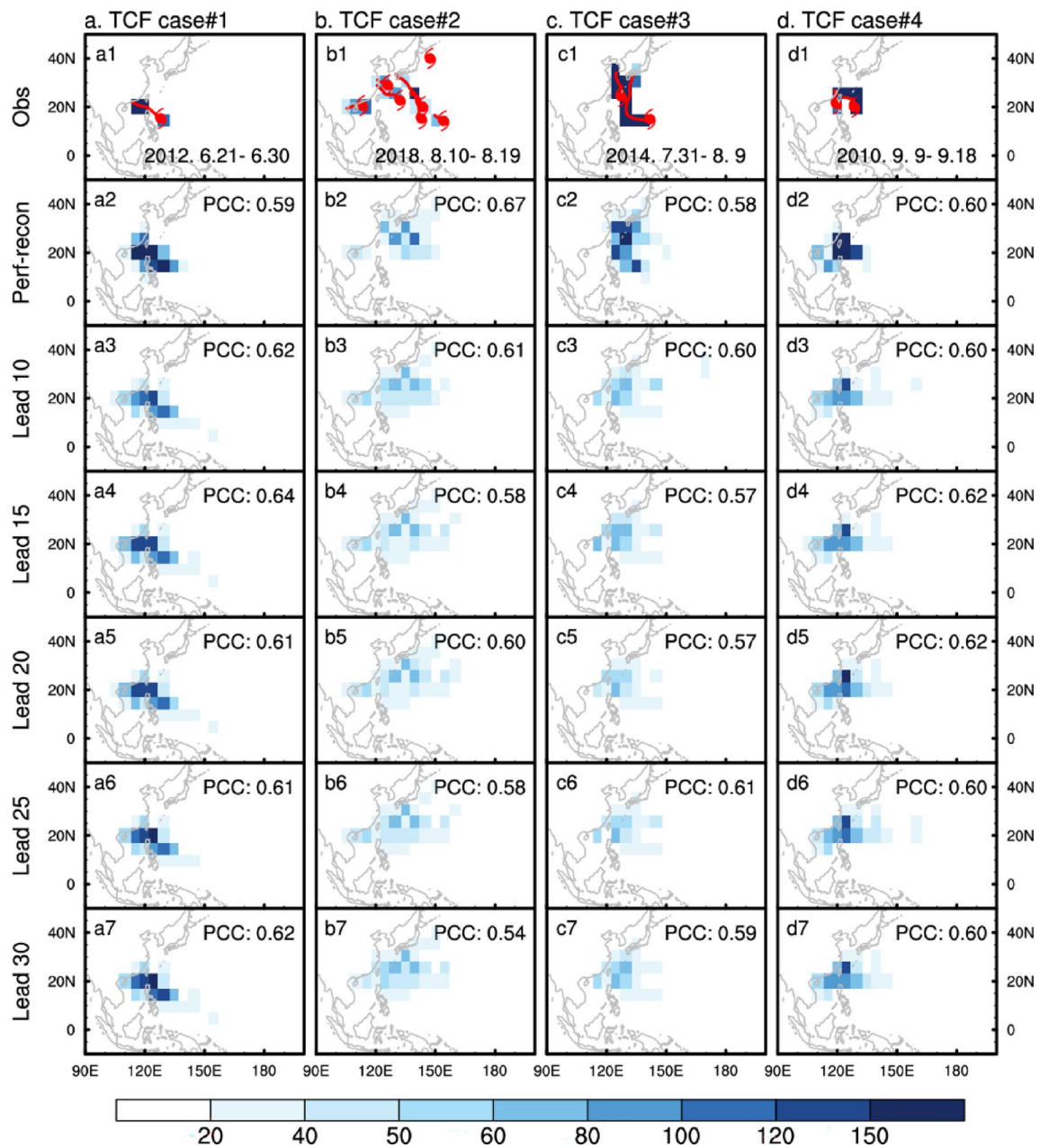


Fig. 15 Four cases of TC frequency (TCF) probability distributions during **a** 21–30 June 2012, **b** 10–19 August 2018, **c** 31 July–9 August 2014, and **d** 9–18 September 2010. From top to bottom: observation, perfect reconstruction, and prediction at leads of 10, 15, 20, 25, and 30 days. The TCF probability at each grid point is defined as the TCF

in each $5^\circ \times 5^\circ$ box divided by the total TC count over the WNP. The red typhoon symbols and curves indicate the observed TC genesis locations and trajectories for each TC case. The pattern correlation coefficients between observations and predictions are shown in the upper-right corner of each panel

factor contributing to the intraseasonal GPI anomalies for all seven clusters. The ISO-related low-level absolute vorticity plays a secondary role. Indeed, these two dominant factors have been documented as important for WNP basin-wide TC genesis in previous studies (Zhao et al. 2015). In addition to the process of TC genesis, we also examined the influences of ISO on the movement of TCs for individual clusters. Accompanied by the intraseasonal cyclonic

anomalies over the TC genesis locations, the background steering flows associated with different clusters vary geographically (Fig. 7). For the straight-moving TCs (C1, C5, and C6), the ISO-related cyclonic flows appear over the SCS and the Philippine Sea in the low latitudes, leading to enhanced easterly flow related to the westward extension of the WNP subtropical high. In contrast, the eastward shift of the WNP subtropical high induced by the strengthened ISO

cyclonic flow favors the recurving TCs of C4 and C7. The results based on background steering flows of different clusters clearly illustrate the ISO effect on TC tracks, supporting previous findings using a composite of relatively limited TC cases (Chen et al. 2009).

Considering the significant influence of ENSO on TC activities at interannual timescales (Wang and Chan 2002; Camargo and Sobel 2005), the different modulation by LF (Fig. 8) and HF (Fig. 9) ISO of the intraseasonal TC genesis in different ENSO phases should also be discussed. Although the total TC counts in the WNP during El Niño and La Niña years are similar, the TCs of individual clusters are significantly influenced by ENSO (Figs. 8, 9). There are more TCs generated in the southeast quadrant of the WNP, such as those of C3, C4, and C6, during El Niño years compared with those of the same clusters during La Niña years. The modulations of HF and LF ISO in some specific phases on the total numbers of TCs over the WNP are different during El Niño and La Niña years, which are changed by the low-level winds associated with ENSO conditions. The modulations of HF and LF ISOs on the TCs generated in the southeast quadrant of the WNP, such as the TCs of C3, C4, and C6, are relatively weaker during La Niña years compared with El Niño years. The modulations of ISOs on land-falling TCs (C5 and C7) are weaker during El Niño years.

Based on these diagnostic results, we developed linear regression models using the ISO-related large-scale fields as predictors for predicting anomalous TC genesis counts (relative to smoothed climatological 10-day-mean TC counts) every 10 days for each cluster and each ENSO phase (Fig. 10). The prediction skill for TC genesis counts, as assessed by the TCC, suggests that the statistical model has the capability of predicting anomalous TC genesis numbers at the lead time of 30 days, which is superior to the prediction skills of models that do not consider the effects of ENSO (Fig. 14). Predicted probability maps of TCF were then constructed by considering the climatological probability distribution of each cluster (Kim et al. 2012). The predicted distributions of TCF (Fig. 15) should provide useful information for disaster prevention and mitigation.

The predictability sources of these statistical TC forecast models are from the intraseasonal variabilities of large-scale fields associated with TC genesis (GPI components), while other potential sources of predictability, such as high-frequency equatorial waves (Frank and Roundy 2006; Schreck et al. 2012; Lai et al. 2020) and extratropical–tropical interaction (Camargo et al. 2019), need more exploration, which could potentially lead to improvements in TC subseasonal forecasting. In addition, not only the TC genesis and frequency distribution over the WNP, but also TC forecast products, including TC intensity and ACE, need further exploration.

Author contributions YQ performed the research and analyzed the data; P-CH designed the research; YQ and P-CH wrote the manuscript; HM, JG, HW, and MD revised the manuscript.

Funding This work was supported by the National Natural Science Foundation of China (42205024), the National Postdoctoral Program for Innovative Talent (BX2021133), the China Postdoctoral Science Foundation of No. 70 General Fund (2021M701753), and the Natural Science Foundation of Jiangsu Province, China (BK20220459). We acknowledge the High-Performance Computing Center of Nanjing University of Information Science & Technology for their support of this work.

Data availability The Regional Specialized Meteorological Centers Tokyo-Typhoon Center best-track dataset is available at <https://www.jma.go.jp/jma/eng/jma-center/rsmc-hp-pub-eg/trackarchives.html>. All reanalysis data used in this study were obtained from publicly available sources. The ECMWF ERA-Interim product is available at <https://apps.ecmwf.int/datasets/data/interim-full-daily/levtype=pl/>. The NOAA High-resolution Blended Analysis of daily SST can be found at <https://psl.noaa.gov/data/gridded/data.noaa.oisst.v2.highres.html>. NOAA daily OLR can be found at https://psl.noaa.gov/data/gridded/data.uninterp_OLR.html. The real-time NMME forecast Niño-3.4 index is available at https://ftp.cpc.ncep.noaa.gov/NMME/realtime_anom/ENSMEAN/.

Declarations

Conflict of interest The authors declare that they have no conflicts of interest.

Ethical approval Not applicable to this article.

References

- Bell GD, Halpert MS, Schnell RC et al (2000) The 1999 North Atlantic and eastern North Pacific hurricane season [in “Climate Assessment for 1999”]. *Bull Am Meteorol Soc* 81:S19–S22
- Bezdek JC (1981) Pattern recognition with fuzzy objective function algorithms. Kluwer Academic, Boston
- Bister M, Emanuel KA (1998) Dissipative heating and hurricane intensity. *Meteorol Atmos Phys* 65:233–240. <https://doi.org/10.1007/BF01030791>
- Camargo SJ, Barnston AG (2009) Experimental dynamical seasonal forecasts of tropical cyclone activity at IRI. *Weather Forecast* 24:472–491. <https://doi.org/10.1175/2008WAF2007099.1>
- Camargo SJ, Sobel AH (2005) Western North Pacific tropical cyclone intensity and ENSO. *J Clim* 18:2996–3006
- Camargo SJ, Robertson AW, Gaffney SJ et al (2007a) Cluster analysis of typhoon tracks. Part II: large-scale circulation and ENSO. *J Clim* 20:3654–3676. <https://doi.org/10.1175/JCLI4203.1>
- Camargo SJ, Robertson AW, Gaffney SJ et al (2007b) Cluster analysis of typhoon tracks. Part I. General properties. *J Clim* 20:3635–3653. <https://doi.org/10.1175/JCLI4188.1>
- Camargo SJ, Wheeler MC, Sobel AH (2009) Diagnosis of the MJO modulation of tropical cyclogenesis using an empirical index. *J Atmos Sci* 66:3061–3074. <https://doi.org/10.1175/2009JAS3101.1>
- Camargo SJ, Camp J, Elsberry RL et al (2019) Tropical cyclone prediction on subseasonal time-scales. *Trop Cyclone Res Rev* 8:150–165. <https://doi.org/10.6057/2019TCRR03.04>
- Chen T-C, Wang S-Y, Yen M-C, Clark AJ (2009) Impact of the intraseasonal variability of the western North Pacific large-scale

- circulation on tropical cyclone tracks. *Weather Forecast* 24:646–666. <https://doi.org/10.1175/2008WAF2222186.1>
- Chia H-H, Ropelewski CF (2002) The interannual variability in the genesis location of tropical cyclones in the northwest Pacific. *J Clim* 15:2934–2944. [https://doi.org/10.1175/1520-0442\(2002\)015%3c2934:TIVITG%3e2.0.CO;2](https://doi.org/10.1175/1520-0442(2002)015%3c2934:TIVITG%3e2.0.CO;2)
- Chu P-S, Zhao X, Ho C-H et al (2010) Bayesian forecasting of seasonal typhoon activity: a track-pattern-oriented categorization approach. *J Clim* 23:6654–6668. <https://doi.org/10.1175/2010JCLI3710.1>
- Dee DP, Uppala SM, Simmons AJ et al (2011) The ERA-Interim reanalysis: configuration and performance of the data assimilation system. *Q J R Meteorol Soc* 137:553–597. <https://doi.org/10.1002/qj.828>
- Duchon CE (1979) Lanczos filtering in one and two dimensions. *J Appl Meteorol* 18:1016–1022
- Elsberry RL, Jordan MS, Vitart F (2010) Predictability of tropical cyclone events on intraseasonal timescales with the ECMWF monthly forecast model. *Asia Pac J Atmos Sci* 46:135–153. <https://doi.org/10.1007/s13143-010-0013-4>
- Emanuel K (1995) Sensitivity of tropical cyclones to surface exchange coefficients and revised steady-state model incorporating eye dynamics. *J Atmos Sci* 52:3969–3976
- Frank WM, Roundy PE (2006) The role of tropical waves in tropical cyclogenesis. *Mon Weather Rev* 134:2397–2417. <https://doi.org/10.1175/MWR3204.1>
- Gao J, Li T (2011) Factors controlling multiple tropical cyclone events in the western North Pacific. *Mon Weather Rev* 139:885–894. <https://doi.org/10.1175/2010MWR3340.1>
- Gray WM (1968) Global view of the origin of tropical disturbances and storms. *Mon Weather Rev* 96:669–700. [https://doi.org/10.1175/1520-0493\(1968\)096%3c0669:gvotoo%3e2.0.co;2](https://doi.org/10.1175/1520-0493(1968)096%3c0669:gvotoo%3e2.0.co;2)
- Gray WM, Landsea CW, Mielke PW, Berry KJ (1992) Predicting Atlantic seasonal hurricane activity 6–11 months in advance. *Weather Forecast* 7:440–455
- Gray WM, Landsea CW, Mielke PW, Berry KJ (1993) Predicting Atlantic basin seasonal tropical cyclone activity by 1 August. *Weather Forecast* 8:73–86
- Gray WM, Landsea C, Mielke P, Berry K (1994) Predicting Atlantic basin seasonal tropical cyclone activity by 1 June. *Weather Forecast* 9:103–115
- Gregory PA, Camp J, Bigelow K et al (2019) Sub-seasonal predictability of the 2017–2018 Southern Hemisphere tropical cyclone season. *Atmos Sci Lett* 20:e886. <https://doi.org/10.1002/asl.886>
- Han X, Zhao H, Li X, Raga GB, Wang C (2020) Modulation of boreal extended summer tropical cyclogenesis over the Northwest Pacific by the quasi-biweekly oscillation under different El Niño–southern oscillation phases. *Int J Climatol* 40(2):858–873. <https://doi.org/10.1002/joc.6244>
- Hsu P-C, Li T, Tsou C-H (2011) Interactions between boreal summer intraseasonal oscillations and synoptic-scale disturbances over the western North Pacific. Part I: energetics diagnosis. *J Clim* 24:927–941. <https://doi.org/10.1175/2010JCLI3833.1>
- Hsu P-C, Li T, You L et al (2015) A spatial-temporal projection model for 10–30 day rainfall forecast in South China. *Clim Dyn* 44:1227–1244. <https://doi.org/10.1007/s00382-014-2215-4>
- Jiang X, Zhao M, Waliser DE (2012) Modulation of tropical cyclones over the Eastern Pacific by the intraseasonal variability simulated in an AGCM. *J Clim* 25:6524–6538. <https://doi.org/10.1175/JCLI-D-11-00531.1>
- Jiang X, Xiang B, Zhao M et al (2018) Intraseasonal tropical cyclogenesis prediction in a global coupled model system. *J Clim* 31:6209–6227. <https://doi.org/10.1175/JCLI-D-17-0454.1>
- Keshavamurty RN (1971) Power spectra of large-scale disturbances of Indian summer monsoon. *Bull Am Meteorol Soc* 52:796
- Keshavamurty RN (1972) On the vertical tilt of monsoon disturbances. *J Atmos Sci* 29:993–995
- Kim J-H, Ho C-H, Kim H-S et al (2008) Systematic variation of summertime tropical cyclone activity in the western North Pacific in relation to the Madden-Julian oscillation. *J Clim* 21:1171–1191. <https://doi.org/10.1175/2007JCLI1493.1>
- Kim H-S, Kim J-H, Ho C-H, Chu P-S (2011) Pattern classification of typhoon tracks using the fuzzy *c*-means clustering method. *J Clim* 24:488–508. <https://doi.org/10.1175/2010JCLI3751.1>
- Kim H-S, Ho C-H, Kim J-H, Chu P-S (2012) Track-pattern-based model for seasonal prediction of tropical cyclone activity in the western North Pacific. *J Clim* 25:4660–4678. <https://doi.org/10.1175/JCLI-D-11-00236.1>
- Kirtman BP, Min D, Infanti JM (2014) The North American multimodel ensemble: phase-1 seasonal-to-interannual prediction; phase-2 toward developing intraseasonal prediction. *Bull Am Meteorol Soc* 95:585–601. <https://doi.org/10.1175/BAMS-D-12-00050.1>
- Klotzbach PJ (2008) Refinements to Atlantic basin seasonal hurricane prediction from 1 December. *J Geophys Res Atmos* 113:1–11. <https://doi.org/10.1029/2008JD010047>
- Klotzbach PJ, Gray WM (2004) Updated 6–11-month prediction of Atlantic basin seasonal hurricane activity. *Weather Forecast* 19:917–934. [https://doi.org/10.1175/1520-0434\(2004\)019%3c0917:UMPOAB%3e2.0.CO;2](https://doi.org/10.1175/1520-0434(2004)019%3c0917:UMPOAB%3e2.0.CO;2)
- Klotzbach PJ, Gray WM (2009) Twenty-five years of Atlantic basin seasonal hurricane forecasts (1984–2008). *Geophys Res Lett* 36:1–5. <https://doi.org/10.1029/2009GL037580>
- Knapp KR, Kruk MC, Levinson DH et al (2010) The international best track archive for climate stewardship (IBTrACS): unifying tropical cyclone best track data. *Bull Am Meteorol Soc* 91:363–376. <https://doi.org/10.1175/2009BAMS2755.1>
- Lai Q, Gao J, Zhang W, Guan X (2020) Influences of the equatorial waves on multiple tropical cyclone genesis over the western North Pacific. *Terr Atmos Ocean Sci* 31:227–238. <https://doi.org/10.3319/TAO.2020.03.20.01>
- Lee C-Y, Camargo SJ, Vitart F et al (2018) Subseasonal tropical cyclone genesis prediction and MJO in the S2S dataset. *Weather Forecast* 33:967–988. <https://doi.org/10.1175/WAF-D-17-0165.1>
- Leroy A, Wheeler MC (2008) Statistical prediction of weekly tropical cyclone activity in the southern hemisphere. *Mon Weather Rev* 136:3637–3654. <https://doi.org/10.1175/2008MWR2426.1>
- Liebmann B, Smith CA (1996) Description of a complete (interpolated) outgoing longwave radiation dataset. *Bull Am Meteorol Soc* 77:1275–1277
- Li RCY, Zhou W (2013a) Modulation of western North Pacific tropical cyclone activity by the ISO. Part I: genesis and intensity. *J Clim* 26:2904–2918. <https://doi.org/10.1175/JCLI-D-12-00210.1>
- Li RCY, Zhou W (2013b) Modulation of western North Pacific tropical cyclone activity by the ISO. Part II: tracks and landfalls. *J Clim* 26:2919–2930. <https://doi.org/10.1175/JCLI-D-12-00211.1>
- Li RCY, Zhou W, Chan JCL (2012) Asymmetric modulation of western North Pacific cyclogenesis by the Madden-Julian Oscillation under ENSO conditions. *J Clim* 25:5374–5385. <https://doi.org/10.1175/JCLI-D-11-00337.1>
- Liebmann B, Hendon H, Glick D (1994) The relationship between tropical cyclones of the eastern Pacific and Indian Oceans and the Madden-Julian oscillation. *J Meteorol Soc Japan* 72:401–411
- Madden RA, Julian PR (1971) Detection of a 40–50-day oscillation in the zonal wind in the tropical Pacific. *J Atmos Sci* 28:702–708
- Madden RA, Julian PR (1972) Description of global-scale circulation cells in the tropics with a 40–50-day period. *J Atmos Sci* 29:1109–1123
- McBride JL (1995) Tropical cyclone formation. In: Russel Elsberry (ed) *Global perspective on tropical cyclones*, Geneva. World Meteorological Organization Rep. TCP-38, WMO/TD-No 693, pp 63–105

- Murakami H, Wang B (2010) Future change of North Atlantic tropical cyclone tracks: projection by a 20-km-mesh global atmospheric model. *J Clim* 23:2699–2721. <https://doi.org/10.1175/2010JCLI3338.1>
- Murakami H, Vecchi GA, Underwood SD et al (2015) Simulation and prediction of category 4 and 5 hurricanes in the high-resolution GFDL HiFLOR coupled climate model. *J Clim* 28:9058–9079. <https://doi.org/10.1175/JCLI-D-15-0216.1>
- Murakami H, Vecchi GA, Villarini G et al (2016a) Seasonal forecasts of major hurricanes and landfalling tropical cyclones using a high-resolution GFDL coupled climate model. *J Clim* 29:7977–7989. <https://doi.org/10.1175/JCLI-D-16-0233.1>
- Murakami H, Villarini G, Vecchi GA et al (2016b) Statistical-dynamical seasonal forecast of North Atlantic and U.S. landfalling tropical cyclones using the high-resolution GFDL FFLOR coupled model. *Mon Weather Rev* 144:2101–2123. <https://doi.org/10.1175/MWR-D-15-0308.1>
- Murakami H, Vecchi GA, Delworth TL et al (2017) Dominant role of subtropical pacific warming in extreme Eastern Pacific hurricane seasons: 2015 and the future. *J Clim* 30:243–264. <https://doi.org/10.1175/JCLI-D-16-0424.1>
- Nakano M, Kubota H, Miyakawa T, Satoh M (2017) Genesis of super cyclone Pam (2015): modulation of low-frequency large-scale circulations and the Madden-Julian oscillation by sea surface temperature anomalies. *Mon Weather Rev* 145:3143–3159. <https://doi.org/10.1175/MWR-D-16-0208.1>
- North GR, Bell TL, Cahalan RF, Moeng FJ (1982) Sampling errors in the estimation of empirical orthogonal functions. *Mon Weather Rev* 110:699–706. [https://doi.org/10.1175/1520-0493\(1982\)110%3c0699:SEITEO%3e2.0.CO;2](https://doi.org/10.1175/1520-0493(1982)110%3c0699:SEITEO%3e2.0.CO;2)
- Pielke RA, Gratz J, Landsea CW et al (2008) Normalized hurricane damage in the United States: 1900–2005. *Nat Hazards Rev* 9:29–42. [https://doi.org/10.1061/\(ASCE\)1527-6988\(2008\)9:1\(29\)](https://doi.org/10.1061/(ASCE)1527-6988(2008)9:1(29))
- Qian Y, Hsu PC, Murakami H, Xiang B, You L (2020) A hybrid dynamical-statistical model for advancing subseasonal tropical cyclone prediction over the western North Pacific. *Geophys Res Lett* 47:e2020GL090095. <https://doi.org/10.1029/2020GL090095>
- Reynolds RW, Smith TM, Liu C et al (2007) Daily high-resolution-blended analyses for sea surface temperature. *J Clim* 20:5473–5496. <https://doi.org/10.1175/2007JCLI1824.1>
- Satoh M, Oouchi K, Nasuno T et al (2012) The Intra-Seasonal Oscillation and its control of tropical cyclones simulated by high-resolution global atmospheric models. *Clim Dyn* 39:2185–2206. <https://doi.org/10.1007/s00382-011-1235-6>
- Schreck CJ, Molinari J, Aiyyer A (2012) A global view of equatorial waves and tropical cyclogenesis. *Mon Weather Rev* 140:774–788. <https://doi.org/10.1175/MWR-D-11-00110.1>
- Slade SA, Maloney ED (2013) An intraseasonal prediction model of atlantic and east Pacific tropical cyclone genesis. *Mon Weather Rev* 141:1925–1942. <https://doi.org/10.1175/MWR-D-12-00268.1>
- Smith AB, Katz RW (2013) US billion-dollar weather and climate disasters: data sources, trends, accuracy and biases. *Nat Hazards* 67:387–410. <https://doi.org/10.1007/s11069-013-0566-5>
- Stoica P, Moses RL (2005) Introduction to spectral analysis. Prentice Hall Inc, Upper Saddle River
- Vitar F, Leroy A, Wheeler MC (2010) A comparison of dynamical and statistical predictions of weekly tropical cyclone activity in the Southern Hemisphere. *Mon Weather Rev* 138:3671–3682. <https://doi.org/10.1175/2010MWR3343.1>
- Wang B, Chan JCL (2002) How strong ENSO events affect tropical storm activity over the western North Pacific. *J Clim* 15:1643–1658. [https://doi.org/10.1175/1520-0442\(2002\)015%3c1643:HSEAT%3e2.0.CO;2](https://doi.org/10.1175/1520-0442(2002)015%3c1643:HSEAT%3e2.0.CO;2)
- Wei X, Yang Y, Chen L (2021) The extended-range forecast of tropical cyclogenesis over the South China Sea based on the intraseasonal oscillation. *Meteorol Atmos Phys* 133:1577–1589. <https://doi.org/10.1007/s00703-021-00830-0>
- Xiang B, Zhao M, Jiang X et al (2015) The 3–4-week MJO prediction skill in a GFDL coupled model. *J Clim* 28:5351–5364. <https://doi.org/10.1175/JCLI-D-15-0102.1>
- Zhang W, Vecchi GA, Murakami H et al (2016a) The Pacific meridional mode and the occurrence of tropical cyclones in the western North Pacific. *J Clim* 29:381–398. <https://doi.org/10.1175/JCLI-D-15-0282.1>
- Zhang W, Villarini G, Vecchi GA et al (2016b) Statistical-dynamical seasonal forecast of western North Pacific and East Asia landfalling tropical cyclones using the high-resolution GFDL FFLOR coupled model. *J Adv Model Earth Syst* 8:1289–1309. <https://doi.org/10.1002/2013MS000282>
- Zhao H, Jiang X, Wu L (2015) Modulation of northwest Pacific tropical cyclone genesis by the intraseasonal variability. *J Meteorol Soc Jpn* 93:81–97. <https://doi.org/10.2151/jmsj.2015-006>
- Zhao J, Zhan R, Wang Y et al (2018) Contribution of the Interdecadal Pacific Oscillation to the recent abrupt decrease in tropical cyclone genesis frequency over the western North Pacific since 1998. *J Clim* 31:8211–8224. <https://doi.org/10.1175/JCLI-D-18-0202.1>
- Zhao H, Lu Y, Jiang X, Klotzbach PJ, Wu L, Cao J (2022) A Statistical intraseasonal prediction model of extended boreal summer western North Pacific tropical cyclone genesis. *J Clim* 35:2460–2478. <https://doi.org/10.1175/JCLI-D-21-0110.1>

Publisher's Note Springer Nature remains neutral with regard to jurisdictional claims in published maps and institutional affiliations.

Springer Nature or its licensor (e.g. a society or other partner) holds exclusive rights to this article under a publishing agreement with the author(s) or other rightsholder(s); author self-archiving of the accepted manuscript version of this article is solely governed by the terms of such publishing agreement and applicable law.